
A WELL BALANCED FVC SCHEME FOR 2D SHALLOW WATER FLOWS ON UNSTRUCTURED TRIANGULAR MESHES

Moussa Ziggaf^{a,b,c*}, Imad Kissami^b, Mohamed Boubekeur^c

^a ENSAO, LMCS, Complexe Universitaire, B.P. 669, 60000 Oujda, Morocco

^b MSDA, Mohammed VI Polytechnic University Lot 660, 43150 Ben Guerir, Maroc

^c Université Sorbonne Paris Nord, LAGA, CNRS, UMR 7539, F-93430, Villetaneuse, France

ABSTRACT

We consider in this work the numerical resolution of a 2D shallow water system with a Coriolis effect and bottom friction stresses on unstructured meshes by a new Finite Volume Characteristics (FVC) scheme, which has been introduced in the preliminary works that will be cited below. Our main goal is to extend this approach to 2D unstructured formalism while preserving the physical and mathematical properties of the system, including the C-property.

First, we present our extension by preserving the advantages of the finite volume discretization such as conservation property and the method of characteristics such as elimination of Riemann solvers. Afterward, an approach was applied to the topography source term that leads to a well-balanced scheme satisfying the steady-state condition of still water. A semi-implicit treatment will also be presented in this study to avoid stability problems for the other source terms. Finally, the proposed finite volume method is verified on several benchmark tests and shows good agreement with analytical solutions and experimental results; moreover, it gives a noticeable accuracy and rapidity improvement compared to the original approaches.

Keywords Shallow water flow · Method of characteristics · FVC scheme · Finite volume method · Well-balanced scheme

1 Introduction

Water is a crucial issue for poverty reduction, sustainable development, and achieving the Millennium Development Goals. However, until now, some 2.1 billion people, or 30% of the world's population, still do not have access to a safe water supply (www.who.int/news/18-06-2019). Climate change and uncontrollable human activities cause flood accidents to become more frequent in recent decades. As a result, integrated water resources management is necessary and even indispensable for preventing floods and droughts. The preservation of the environment, the prevention, and control of the impact of natural risks are at the heart of major socio-economic issues.

In water resources management, numerical modelling is still an essential tool, and we can cite numerous numerical modelling applications of free surface flows to the management of water resources, environmental and ecosystem protection: simulation of flows due to a dam break, diversions of floods from a river to a water retention area, the change process of a river bed simulation, sediment or pollutant transport simulation in estuary and coastal environments, (see e.g. [1, 2, 3] etc.). In rivers, estuaries and coastal areas, flows are characterized by: great topographical and morphological complexity, strong affection, or even pure advection in the case of a dam break on a flat and slippery bottom (without friction), a variable space scale (starting from a dozen to a few thousand meters) and in time scale (starting from a few minutes to several days).

Consequently, when developing a numerical approach to solve a free surface flow or other models, one encounters major difficulties which result from the physical complexity of the area and numerical calculations. We consider in this paper a derivative as a

*Corresponding (moussa.ziggaf@um6p.ma)

formal first-order approximation of the three-dimensional free surface incompressible Navier–Stokes equations, using the so-called shallow-water assumption [4]. The difficulty in defining accurate numerical schemes for such hyperbolic systems is related to their non-linear behaviour or, more generally, mathematical structure and the physical phenomena they generate. In particular, the presence of a shock front essentially causes numerical oscillations or artificial scattering, which are due to the treatment of the advection terms in the equations governing the transport of the water mass by a standard method of approximation. Another fundamental point is to get schemes that satisfy the preservation of steady states, such as still water equilibrium in the context of the shallow water system. Different approaches to satisfy the well-balanced property have been proposed (see, e.g. [5, 6, 7, 8, 9, 10]), and recent extensions to other types of homogeneous solvers can be found in [11, 12]. The extension of ENO and WENO schemes to shallow water equations has been studied in [13]. Unfortunately, most ENO and WENO schemes that solve real flows correctly are still very computationally expensive. On the other hand, numerical methods based on kinetic reconstructions have been studied in [14], but the complexity of these methods is relevant. However, most of the above mentioned works, even if they are unstructured two-dimensional methods they lead to rather complex and time consuming algorithms. Other approaches are more efficient, but to our knowledge, they are limited to one-dimensional problems or to two-dimensional Cartesian meshes.

Our main objective in the present study is to develop a class of Eulerian-Lagrangian methods and to accurately solve shallow water equations in 2D-unstructured meshes without relying on Riemann solvers. The proposed FVC scheme belongs to the class of methods that employ only physical fluxes and averaged states in their formulations. It can be interpreted as a predictor–corrector scheme. In the corrector stage, the considered equations are integrated over an Eulerian time–space control volume, whereas, in the predictor stage, the conservation laws are rewritten in an advective form and integrated along the characteristics defined by the advection velocity field. This approach has shown its effectiveness through several test cases represented in the works, [15, 16, 17], but the authors of these three papers remained limited in the Cartesian mesh formalism but, as I have mentioned before, the real problems are characterised by a great topographical and geometrical complexity, hence, the limit of this formalism. A more thorough study of the accuracy of this finite volume discretization method on unstructured meshes was always the objective in these works (see the conclusions of [16, 17]). Therefore, the unstructured finite volume method doesn't only ensure the conservation of mass, which is an important property in the computation of fluid flows but also allows the complex geometry of the computational domain to be perfectly taken into account. For these reasons, we propose an extension of this scheme in an unstructured mesh.

Another strong point of this discretization method is that the Jacobian matrix of the system that caused the slowness of many approximation schemes is not involved in the calculation. Note also that many approximation schemes in the framework of conservation laws require a solver for the Riemann problem at each time step to reconstruct the numerical flow, which is completely avoided in our FVC scheme. Simply this approach is based on a combination of the characteristics method and a finite volume method. Unlike traditional finite volume methods, this technique integrates our equations along the characteristics curves so that numerical flux are easily calculated. We noticed that this approach has several advantages over others conservation law solution techniques. Indeed, the main features of such a finite volume Eulerian-Lagrangian scheme are on the one hand, the capability to satisfy the conservation property resulting in numerical solutions free from spurious oscillations, and on the other hand, the achievement of strong stability and high accuracy for numerical solutions containing shocks or discontinuities.

We first present a projection of the shallow water system in order to find a form of a transport equation on which we will apply the techniques of the characteristics method for the purpose of evaluating our unknowns at the interfaces of our unstructured mesh. We also present original developments to take into account boundary conditions, to reduce the diffusion of the scheme or to increase the efficiency of the method.

Second, we announce a new reformulation of the FVC scheme adapted to non-uniform triangular mesh "unstructured mesh" as well as the discretization of the flow gradients and source terms while keeping the equilibrium and the C-property. It will also be seen that the proposed scheme has the ability to handle calculations of slowly varying flows as well as rapidly varying flows over continuous and discontinuous bottom beds.

This article is organized as follows: Section 2 will be devoted to the presentation of the mathematical model and its projected velocity system, as well as its mathematical and physical properties. In Section 3, numerical methods are formulated for the reconstruction of the finite volume characteristics scheme on an unstructured meshes and the approximation of the source terms keeping the scheme Well-balanced. Section 4 is devoted to the numerical results of several test examples and some results interpretations. It is shown that our new approach achieves the expected accuracy and robustness. Section 5 contains concluding remarks and an outlook. Subsequently, the details of some calculations are written in Appendix.

2 Mathematical Model

2.1 The shallow water model for the free-surface flow

The 2D shallow water system for the free-surface flow with the Coriolis effect and bottom friction stress is formulated as

$$\begin{cases} \partial_t h + \nabla \cdot (h\mathbf{u}) = 0 \\ \partial_t h\mathbf{u} + \nabla \cdot (h\mathbf{u} \otimes \mathbf{u}) + \frac{1}{2} \nabla (gh^2) = -gh\nabla Z - f_c \times h\mathbf{u} - r(h, \mathbf{u}), \end{cases} \quad (1)$$

where the unknowns are always the water height $h(t, x, y) \geq 0$ and the horizontal speed mean $\mathbf{u}(t, x, y) = (u, v)^T(t, x, y) \in \mathbb{R}^2$. The parameter f_c is linked to the angular speed of the earth's rotation, g is the gravitational acceleration, $r(h, \mathbf{u})$ has various expressions, for example, the asymptotic derivation mentioned in [18] leads the authors to consider, at first order, a linear friction term. The quadratic form in the Manning-Strickler velocity is nevertheless the most widely used in river flow applications [19, 20], so in this study we use the latter approximation such that the bottom's friction term $r(h, \mathbf{u})$ is given by, $r(h, \mathbf{u}) = (r_{f_x}, r_{f_y}) := \eta^2 gh^{-1/3} |\mathbf{u}| \mathbf{u}$, such as η is the Manning roughness. The function $Z(x, y)$ represents the bottom profile, see the Fig.1.

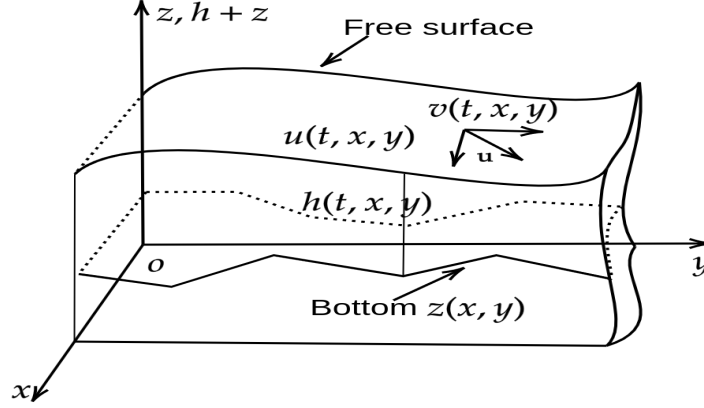


Fig. 1. Illustration of shallow water model variables.

In order to give the reader a global view on the shallow water system we propose to add other aspects in the right hand side of the second equation of system (1). For example we can add the wind's effect on the free surface, i.e. in the case where the wind is moving with high speed there is the friction term $\tau(h, \check{\mathbf{u}})$ which is not negligible. The viscosity or diffusion term can also be added if we want to solve turbulence problems in free surface flow (see e.g [21]). In this case, the second equation of system (1) becomes

$$\partial_t h\mathbf{u} + \nabla \cdot (h\mathbf{u} \otimes \mathbf{u}) + \frac{1}{2} \nabla (gh^2) = -gh\nabla Z - f_c \times h\mathbf{u} - r(h, \mathbf{u}) + \tau(h, \check{\mathbf{u}}) + \nu \vec{\Delta} h\mathbf{u}, \quad (2)$$

where, $\tau(h, \check{\mathbf{u}}) = (\tau_{s_x}, \tau_{s_y}) := \frac{1}{2} \check{C}_f |\check{\mathbf{u}}| \check{\mathbf{u}}$, in which $\check{\mathbf{u}} = (\check{u}, \check{v})^T$ represents the wind speed and \check{C}_f is the coefficient of wind friction with water. ν is the diffusion coefficient associated to the term, $\vec{\Delta} h\mathbf{u} := (\Delta(hu), \Delta(hv))^T$.

For simplicity, in this study we will not deal with these two terms ($\tau(h, \check{\mathbf{u}})$ and $\nu \vec{\Delta} h\mathbf{u}$), we rewrite the system (1) in a conservative vectorial form

$$\partial_t W + \nabla \cdot \mathbb{F}(W) = S(W) + Q(W), \quad (3)$$

where, $\mathbb{F}(W) = (F(W), G(W))^T$. Such that, we note A^T is the transpose of a matrix A ,

$$W = \begin{pmatrix} h \\ hu \\ hv \end{pmatrix}, \quad F(W) = \begin{pmatrix} hu \\ hu^2 + \frac{1}{2}gh^2 \\ huv \end{pmatrix}, \quad G(W) = \begin{pmatrix} hv \\ huv \\ hv^2 + \frac{1}{2}gh^2 \end{pmatrix}, \quad S(W) = \begin{pmatrix} 0 \\ -gh\partial_x Z \\ -gh\partial_y Z \end{pmatrix}, \quad Q(W) = \begin{pmatrix} 0 \\ f_c hv - r_{f_x} \\ -f_c hu - r_{f_y} \end{pmatrix}.$$

Note that the equation (3) has to be solved in a bounded spatial domain Ω , with given boundary and initial conditions. In practice, these conditions depend on the phenomenon studied (see the Section 4 where numerical examples are discussed).

2.1.1 Properties of the system

A simple calculation shows that the system is still written in a quasi-linear form

$$\partial_t W + \mathbf{J}_F \partial_x W + \mathbf{J}_G \partial_y W = S(W) + Q(W), \quad (4)$$

where \mathbf{J}_F and \mathbf{J}_G are the Jacobian matrices of the fluxes

$$\mathbf{J}_F = \begin{pmatrix} 0 & 1 & 0 \\ gh - u^2 & 2u & 0 \\ -uv & v & u \end{pmatrix} \quad \text{and} \quad \mathbf{J}_G = \begin{pmatrix} 0 & 0 & 1 \\ -uv & 2v & u \\ gh - v^2 & 0 & 2v \end{pmatrix}.$$

Following the usual techniques [22, 23], we define $\mathbf{J}_{\mathbb{F}}((\alpha_1, \alpha_2)) := \alpha_1 \mathbf{J}_F + \alpha_2 \mathbf{J}_G$. For any $(\alpha_1, \alpha_2) \in \mathbb{R}^2$, the matrix $\mathbf{J}_{\mathbb{F}}((\alpha_1, \alpha_2))$ has three eigenvalues defined by

$$\lambda_1 = \alpha_1 u + \alpha_2 v,$$

$$\lambda_2 = \alpha_1 u + \alpha_2 v + |(\alpha_1, \alpha_2)| \sqrt{gh},$$

$$\lambda_3 = \alpha_1 u + \alpha_2 v - |(\alpha_1, \alpha_2)| \sqrt{gh}.$$

The shallow water system is a first-order hyperbolic system of balance laws, and it is also strictly hyperbolic for $h > 0$ with real and distinct eigenvalues.

•) *Equilibrium*

An important property is related to the source terms, and the most studied balance family is related to the presence of topography's source term: the shallow water system admits non-trivial steady-states. They are characterized by

$$\nabla \cdot \mathbf{h}\mathbf{u} = 0, \quad \nabla \cdot \left(\frac{|\mathbf{u}|^2}{2} + g(h + Z) \right) - \mathbf{u} \nabla \times \mathbf{u} = 0. \quad (5)$$

For flows in complex geometry, it seems very difficult to numerically preserve all two-dimensional balances, except those that correspond to an area at rest and whose characterization is independent of the dimension considered.

$$h + Z = Cst, \quad \mathbf{u} = 0. \quad (6)$$

This particular stationary state, known as the resting lake state, is important because many flows in lakes or coastal bays are perturbations around this balance. Therefore it is essential to prevent numerical anomalies from disrupting the approached solution. However, the preservation of the stationary states at the numerical level is not obvious to be achieved, and even the simplest one is not an exception. In fact, (6) correspond to a balance between flow terms and source terms, whose discretization are not correlated.

There are other categories of stationary states resulting from an equilibrium between the pressure term and the Coriolis term, i.e.

$$g \nabla h + f_c \times \mathbf{u} = 0.$$

For example, at large scales, the atmospheric and oceanic flows bear most of the time the perturbations of this stationary state [24], therefore it is also very important to be represented in the approached solution. This balance presents a complexity added to the balance of the lake at rest because it involves non-zero speeds.

•) *Entropy inequality*

The physical system we are dealing with here is a system of conservation laws, so the energy aspect is very important in this type of system, thus we propose to say a few words on this point in order to provide insight into the treatment of this notion when

constructing approximate solutions under the constraint of preserving certain properties, for example, the decay of energy in the presence of friction source terms.

We call entropy solution to the shallow water system (see [25]), a weak solution which satisfies the following entropy inequality

$$\partial_t E + \nabla \cdot \left(E + \frac{|\mathbf{u}|^2}{2} \right) \leq 0, \quad (7)$$

where E is a mathematical entropy (which is the mechanical energy see [26]), defined as $E(h, \mathbf{u}, Z) = h \frac{|\mathbf{u}|^2}{2} + \frac{gh^2}{2} + ghZ$.

This inequality becomes equality for regular solutions, in the absence of energy loss terms, notably friction, and remains inequality, for admissible discontinuous solutions, resulting from classical calculations; we invite you to read subsection 1.1 in [27]. The mechanical energy, which is easily verified as convex with respect to the conservative variables, thus acts here as a mathematical entropy. In the case of the system without source terms and in the 1D problem, the mechanical energy is only one of the entropies that must be associated with the system for the problem to be properly posed. In 2D, or when the system contains the source terms, there is no longer a complete family of mathematical entropies. Therefore, even if the inequality (7) alone is not sufficient for a rigorous mathematical study, it nevertheless ensures the presence of an additional bound on a certain positive function of the system unknowns and can provide information on the choice of a physical solution. The finite volume scheme presented in section 3 verifies innately the conservation properties. The energy decay property remains more difficult to satisfy.

2.1.2 The initial and the boundary conditions

To obtain a well-posed problem, we add to this system some initial condition and boundary conditions. In this paper, we consider only two types of boundaries: solid walls on which we prescribe a slip condition and fluid limits on which we prescribe one or two conditions depending on the type of flow (subcritical, supercritical). In some cases we use the injection and Neumann homogeneous boundary conditions.

slip wall	no-slip wall	subcritical inflow	subcritical outflow	supercritical inflow	supercritical outflow
$h_r = h_l$	$h_r = h_l$	$h_r = h_b$	$h_r = h_b$	$h_r = h_b$	$h_r = h_l$
$u_r = 0$	$u_r = 0$	$u_r = u_l + \sqrt{g}(\sqrt{h_l} - \sqrt{h_r})$	$u_r = u_l + \sqrt{g}(\sqrt{h_l} - \sqrt{h_r})$	$u_r = u_b$	$u_r = u_l$
$v_r = v_l$	$v_r = 0$	$v_r = 0$	$v_r = 0v_l$	$v_r = 0$	$v_r = v_l$

Here the subscripts r and l denote the right and left states respectively at a boundary cell interface, such as the local values of the Froude number is used to determinate whether the flow is subcritical or supercritical at a given time. The subscript b above denotes prescribed physical boundary values.

3 Finite volume discretization of the model in 2D unstructured formalism

In this section we present the FVC scheme for the discretization of the shallow water system (3). The method consists of two steps and can be interpreted as a predictor-corrector approach. The first step deals with the classical finite volume method, whereas in the second step, the reconstruction of the numerical flux by constructing the intermediate state using the characteristics method [28].

3.1 Discretization

The integral form of the system (3) can be written as

$$\frac{\partial}{\partial t} \int_{\Omega} W dV + \oint_{\partial\Omega} \mathbb{F}(W) \cdot \mathbf{n} d\sigma = \int_{\Omega} (S(W) + Q(W)) dV, \quad (8)$$

where Ω is the domain of interest, $\partial\Omega$ is the boundary surrounding, \mathbf{n} is the normal vector to $\partial\Omega$ in the outward direction, dV and $d\sigma$ are respectively the surface element and the length element. The problem domain is first discretized into a set of triangular cells forming an unstructured computational mesh see Fig.2. The average of conserved variables is stored at the centre of each cell, and the edges of each cell define the faces of a cell control what is called "control volume".

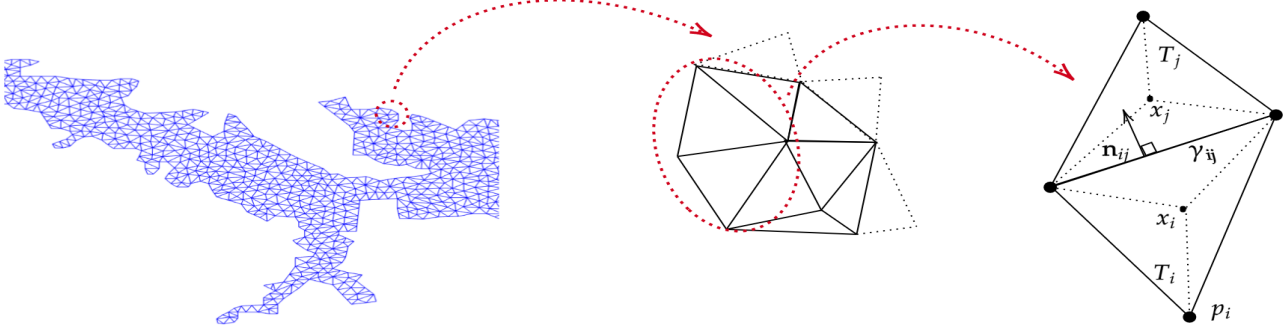


Fig. 2. Generic definition of the Ω domain and the control cells of the mesh.

We use the following notations:

- x_i , centroid of the cell T_i ,
- p_i , vertex of T_i ,
- γ_{ij} , boundary edge between the cells T_i and T_j ,
- $|\gamma_{ij}|$, length of γ_{ij} ,
- $|T_i|$, area of the cell T_i ,
- \mathbf{n}_{ij} , unit normal to γ_{ij} , outward to T_i such as, $\mathbf{n}_{ji} = -\mathbf{n}_{ij}$.

For each triangular control volume, the system (3) is written as

$$|T_i| \frac{dW_i}{dt} + \oint_{\gamma_i} \mathbb{F}(W) \cdot \mathbf{n} d\sigma = \int_{T_i} (S(W) + Q(W)) dV, \quad (9)$$

where W_i is the average quantity of cell T_i stored at the cell centre. The flux vector over each edge of the triangular cell and the discrete form of the integral is

$$\oint_{\gamma_i} \mathbb{F}(W) \cdot \mathbf{n} d\sigma = \sum_{j \in N(i)} |\gamma_{ij}| \Phi(W_{ij}, \mathbf{n}_{ij}),$$

where, $\Phi(W_{ij}, \mathbf{n}_{ij}) \simeq \frac{1}{|\gamma_{ij}|} \int_{\gamma_{ij}} \mathbb{F}(W) \cdot \mathbf{n}_{ij} d\sigma$, is the numerical flux computed at the interface between the cells T_i and T_j .

As explained in the Fig.2, γ_{ij} is the edge surrounding the cell T_i and $N(i)$ is the neighbouring triangles of the cell T_i . The intermediate solution W_{ij} is reconstructed using the FVC scheme. The time discretization of (9) is performed by a first order explicit Euler scheme. The time domain is divided into N sub-intervals $[t_n, t_{n+1}]$ with time step $\Delta t = t_{n+1} - t_n$ for $n = 0, 1, \dots, N$. W^n is the value of a generic function W at time t_n . The fully-discrete formulation of the system (3) is given by

$$W_i^{n+1} = W_i^n - \frac{\Delta t}{|T_i|} \sum_{j \in N(i)} |\gamma_{ij}| \Phi(W_{ij}^n, \mathbf{n}_{ij}) + \Delta t (S_i^n + Q_i^n). \quad (10)$$

3.2 The FVC scheme

In this subsection, we present a generalization of this scheme that was introduced in the preliminary works [16, 28], the first was done in the Cartesian mesh and the second was done without taking into account the source term related to bathymetry and the balance produced by this term. For the corrector stage, we will use 2D finite volume formalism described in Section 3.1. Finally, the predictor stage and the final reformulation of the FVC scheme will be presented in this subsection.

3.2.1 Construction of the projected speed model

Let us discretize the spatial domain Ω with cells T_i as $\overline{\Omega} = \bigcup_{i=1}^{N_{ele}} T_i$ and $\partial T_i = \bigcup_{j \in N(i)} \gamma_{ij}$,

with, ∂T_i is the border of the cell T_i and N_{ele} is the total number of element.

Integrating the equations (1) over the cell T_i , the basic equations of the finite volume method obtained using the divergence theorem are given by

$$\frac{\partial}{\partial t} \int_{T_i} h \, dV + \int_{\partial T_i} h u_\eta \, d\sigma = 0, \quad (11a)$$

$$\frac{\partial}{\partial t} \int_{T_i} h u \, dV + \int_{\partial T_i} \left\{ h u u_\eta + \frac{1}{2} g h^2 n_x \right\} d\sigma = \int_{\partial T_i} -g h Z n_x \, d\sigma + \int_{T_i} f_c h v \, dV - \int_{T_i} \eta^2 g h u \frac{|\mathbf{u}|}{h^{4/3}} \, dV, \quad (11b)$$

$$\frac{\partial}{\partial t} \int_{T_i} h v \, dV + \int_{\partial T_i} \left\{ h v u_\eta + \frac{1}{2} g h^2 n_y \right\} d\sigma = \int_{\partial T_i} -g h Z n_y \, d\sigma - \int_{T_i} f_c h u \, dV - \int_{T_i} \eta^2 g h v \frac{|\mathbf{u}|}{h^{4/3}} \, dV, \quad (11c)$$

where $\eta = (n_x, n_y)^T$ the unit outward normal to the surface $|T_i|$ of the cell T_i and tangential $\tau = (-n_y, n_x)^T$ where the normal velocity $u_\eta = u n_x + v n_y$ and the tangential velocity $u_\tau = v n_x - u n_y$ (see Fig.3). In order to simplify the system (11), we do the following operations

$12b \leftarrow n_x 11b + n_y 11c$, $12c \leftarrow n_x 11c - n_y 11b$. The outcome of these operations is

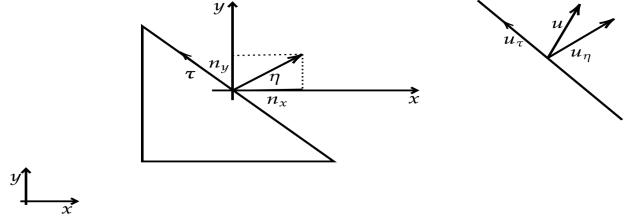


Fig. 3. The projected velocity on the control volume.

$$\frac{\partial}{\partial t} \int_{T_i} h \, dV + \int_{\partial T_i} h u_\eta \, d\sigma = 0, \quad (12a)$$

$$\frac{\partial}{\partial t} \int_{T_i} h u_\eta \, dV + \int_{\partial T_i} \left\{ h u_\eta^2 + \frac{1}{2} g h^2 \right\} d\sigma = - \int_{\partial T_i} g h Z \, d\sigma + \int_{T_i} f_c h u_\tau \, dV - \int_{T_i} \eta^2 g h u_\eta \frac{|\mathbf{u}|}{h^{4/3}} \, dV, \quad (12b)$$

$$\frac{\partial}{\partial t} \int_{T_i} h u_\tau \, dV + \int_{\partial T_i} h u_\tau u_\eta \, d\sigma = - \int_{T_i} f_c h u_\eta \, dV - \int_{T_i} \eta^2 g h u_\tau \frac{|\mathbf{u}|}{h^{4/3}} \, dV, \quad (12c)$$

which can be rewritten the system (12) in a differential form as

$$\begin{cases} \frac{\partial h}{\partial t} + \frac{\partial h u_\eta}{\partial \eta} = 0, \\ \frac{\partial h u_\eta}{\partial t} + \frac{\partial}{\partial \eta} \left(h u_\eta^2 + \frac{1}{2} g h^2 \right) = -g h \partial_\eta Z + f_c h u_\tau - \eta^2 g h u_\eta \frac{|\mathbf{u}|}{h^{4/3}}, \\ \frac{\partial h u_\tau}{\partial t} + \frac{\partial}{\partial \eta} (h u_\eta u_\tau) = -f_c h u_\eta - \eta^2 g h u_\tau \frac{|\mathbf{u}|}{h^{4/3}}. \end{cases} \quad (13)$$

The system (13) can also be reformulated in the transport equation form as

$$\frac{\partial \mathbf{U}}{\partial t}(t, X) + u_\eta(t, X) \frac{\partial \mathbf{U}}{\partial \eta}(t, X) = \mathbf{F}(\mathbf{U}, Z, f_c) \quad \forall X = (x, y) \in \Omega \subset \mathbb{R}^2, \quad t > t_0, \quad (14)$$

where,

$$\mathbf{U} = \begin{pmatrix} h \\ h u_\eta \\ h u_\tau \end{pmatrix}, \quad \mathbf{F}(\mathbf{U}, Z, f_c) = \begin{pmatrix} -h \partial_\eta (u_\eta) \\ -g h \partial_\eta (h + Z) + f_c h u_\tau - h u_\eta \partial_\eta (u_\eta) - \eta^2 g h u_\eta \frac{|\mathbf{u}|}{h^{4/3}} \\ -f_c h u_\eta - h u_\tau \partial_\eta (u_\eta) - \eta^2 g h u_\tau \frac{|\mathbf{u}|}{h^{4/3}} \end{pmatrix}.$$

The aim of using this technique on the local coordinates of the two-dimensional shallow water system (1) in the control volume T_i , is to reduce the dimension to an one-dimensional system (14) on each surface $|T_i|$ of this control volume.

3.2.2 Flux construction

we reconstruct the numerical flux $\Phi(W_{ij}^n, \mathbf{n}_{ij})$ using the method of characteristics. The fundamental idea of this method is to impose a regular grid at the new time level and to backtrack the flow trajectories to the previous time level, for more details see [29, 30]. At the previous time level, the quantities that are needed are evaluated by interpolation from their known values on a irregular grid, we'll see about that later.

3.2.3 Method of characteristics

The characteristic curves associated with the equation (14) are solutions of the following Cauchy problem

$$\begin{cases} \frac{dX^c(t)}{dt} = u_\eta(t, X^c(t)) \cdot \mathbf{n} & t \in [t_n, t_n + \alpha\Delta t], \quad \alpha \in]0, \frac{t_{end} - t_n}{\Delta t}[, \\ X^c(t_n + \alpha\Delta t) = X^*. \end{cases} \quad (15)$$

Note that $X^c(s)$ is the departure point at time s of a particle that will arrive at the interface γ_{ij} in time $t_n + \alpha\Delta t$, see the Fig.4. The method of characteristics does not follow the flow particles forward in time, as the Lagrangian schemes do, instead it traces backwards the position at time t_n of particles that will reach the points of a fixed mesh at time $t_n + \alpha\Delta t$. By doing so, the method avoids the grid distortion difficulties that the conventional Lagrangian schemes have. Hence, the solution of (15) can be expressed in an integral form as

$$X^c(t_n) = X^* - \int_{t_n}^{t_n + \alpha\Delta t} u_\eta(s, X^c(s)) \cdot \mathbf{n} ds, \quad (16)$$

this integral can be calculated using an integral approximation method. In our approach, we used a Runge-Kutta 3 method to approximate the integral in (16) which is accurate enough. In order to complete the reformulation of the algorithm used, the departure points must be calculated once the characteristic curves are known. Therefore, the solution of the transport equation (14) is given by

$$\mathbf{U}(t_n + \alpha\Delta t, X^*) = \mathbf{U}(t_n, X^c(t_n)) + \int_{t_n}^{t_n + \alpha\Delta t} \mathbf{F}(\mathbf{U}(s, X^c(t_n)), Z, f_c) ds, \quad (17)$$

where $\mathbf{U}(t_n, X^c(t_n))$ is the solutions at the characteristic feet computed by the local least squares interpolation method. In other cases, the integral of the equation (17) can be calculated using a first-order approximation based on the rectangle method, the vector \mathbf{U}^n is reconstructed at the interfaces using

$$\mathbf{U}_{ij}^n = \hat{\mathbf{U}}_{ij}^n + \alpha\Delta t \mathbf{F}(\hat{\mathbf{U}}_{ij}^n, Z, f_c), \quad (18)$$

where,

$$\hat{\mathbf{U}}_{ij}^n = \mathbf{U}(t_n, X^c(t_n)) = \sum_{k \in V(c)} \alpha_k(c) \mathbf{U}(X^k), \quad (19)$$

where, $V(c) := \{ \text{the nodes and cell centres around the edge } \gamma_{ij} \}$, see the Fig.5 and $\alpha_k(c)$ is weights coming from the least squares method (LSM). It can be written

$$\alpha_k(c) = \frac{1 + \lambda \cdot (X^k - X^c)}{\text{Card}(V(c)) + \lambda \cdot R}, \quad (20)$$

such as, $\lambda = (\lambda_x, \lambda_y)$ and $R = (R_x, R_y)$. The weights parameters are given by formulas (see the Appendix).

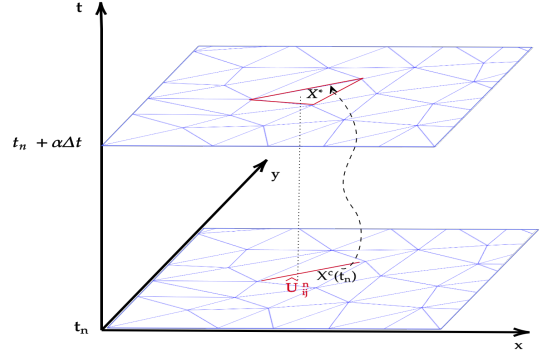


Fig. 4. Illustration of the method of characteristics: An Eulerian gridpoint $X^c(t_n)$ is traced back in time to X^* where the intermediate solution $\hat{\mathbf{U}}_{ij}^n$ is interpolated.

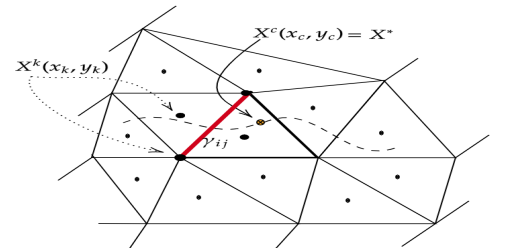


Fig. 5. LSM Illustration.

To approximate $\mathbf{F}(\mathbf{U}, Z, f_c)$, (i.e. $\partial_\eta(u_\eta)$, $\partial_\eta(h + Z)$, ...) we will need to approximate these derivatives in the interfaces, for that we use the diamond cell Fig.6. This cell is constructed by connection of centres of gravity (L, R) of cells T_i, T_j which share the interface γ_{ij} and its endpoints S, N . We obtain the co-volume $SRNL$ by this construction. One can assume that the gradient is constant on the co-volume $SRNL$. According to Green-Gauss theorem the approximation leads to

$$\nabla u_{ij} = \frac{1}{2\mu_{SRNL}} \left\{ (u_S - u_N)\vec{n}_{LR}|\gamma_{LR}| + (u_R - u_L)\vec{n}_{ij}|\gamma_{ij}| \right\}, \quad (21)$$

where u_N, u_S, u_R , and u_L represent respectively the values of the quantity u in the point N, S, R and L . \vec{n}_{LR} is a unit normal vector of the co-volume face γ_{LR} and $|\gamma_{LR}|$ is its length. The others co-volume interfaces and their normal vectors are labeled analogically. μ_{SRNL} is the area of the co-volume $SRNL$. The calculation that gives us the formula (21) is detailed in the Appendix.

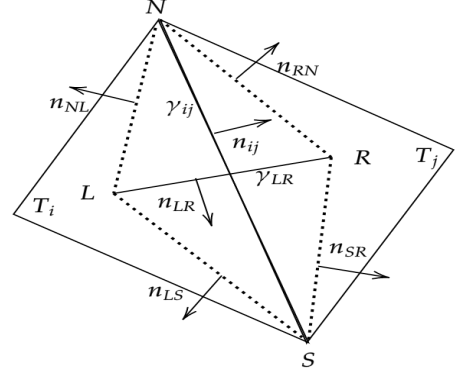


Fig. 6. Diamond cell in 2D

After the discretization of the source terms (see subsection 3.2.4), the district equation system (18) leads to the following predictor step

•) *Predictor stage*

$$\left\{ \begin{array}{l} h_{ij}^n = \hat{h}_{ij}^n - \alpha \Delta t \hat{h}_{ij}^n \nabla (\hat{u}_\eta)_{ij}^n, \\ (hu_\eta)_{ij}^n = (\hat{h}u_\eta)_{ij}^n - \alpha \Delta t \left\{ g \hat{h}_{ij}^n \nabla (\hat{h}_{ij}^n + Z_{ij}) - f_c (\hat{h}u_\tau)_{ij}^n + (\hat{h}u_\eta)_{ij}^n \nabla (\hat{u}_\eta)_{ij}^n + \eta^2 g (\hat{h}u_\eta)_{ij}^n \frac{|\hat{\mathbf{u}}_{ij}^n|}{(\hat{h}^{3/4})_{ij}^n} \right\}, \\ (hu_\tau)_{ij}^n = (\hat{h}u_\tau)_{ij}^n - \alpha \Delta t \left\{ f_c (\hat{h}u_\eta)_{ij}^n + (\hat{h}u_\tau)_{ij}^n \nabla (\hat{u}_\eta)_{ij}^n + \eta^2 g (\hat{h}u_\tau)_{ij}^n \frac{|\hat{\mathbf{u}}_{ij}^n|}{(\hat{h}^{3/4})_{ij}^n} \right\}. \end{array} \right. \quad (22)$$

Once these projected states are calculated, the quantity W_{ij} will be calculated using the following transformations

$$hu_{ij}^n = (hu_\eta)_{ij}^n n_x - (hu_\tau)_{ij}^n n_y, \quad \text{and} \quad hv_{ij}^n = (hu_\tau)_{ij}^n n_x + (hu_\eta)_{ij}^n n_y.$$

•) *Corrector stage*

$$\left\{ \begin{array}{l} W_{ij}^n = (h_{ij}^n \quad hu_{ij}^n \quad hv_{ij}^n)^T, \\ \Phi(W_{ij}^n, \mathbf{n}_{ij}) = \mathbb{F}(W_{ij}^n) \cdot \mathbf{n}_{ij}, \\ W_i^{n+1} = W_i^n - \frac{\Delta t}{|T_i|} \sum_{j \in N(i)} |\gamma_{ij}| \Phi(W_{ij}^n, \mathbf{n}_{ij}) + \Delta t S_i^n + \Delta t Q_i^n. \end{array} \right. \quad (23)$$

3.2.4 Well-balanced FVC scheme: the discretization of the bathymetry source term

In order to be able to calculate realistic flows we now consider the case $\nabla Z \neq 0_{\mathbb{R}^2}$ and introduce a numerical discretization of the source terms. As discussed in paragraph 2.1.1, the treatment of source terms related to bathymetry in the shallow water system poses a challenge in many numerical methods. In our scheme, the approximation of the source term S_i^n is reconstructed in such a way that the C-property [7] is satisfied, i.e. to maintain a discrete local balance of the continuous stationary state in still water.

$$\left. \begin{array}{l} h_i^n + Z_i = h_j^n + Z_j = H := cst \\ \mathbf{u}_i^n + \mathbf{u}_j^n = 0_{\mathbb{R}^2}, \quad \forall T_i, T_j \in \bar{\Omega} \end{array} \right\} \Rightarrow h_i^{n+1} + Z_i = H, \quad \text{and} \quad \mathbf{u}_i^{n+1} = 0_{\mathbb{R}^2}. \quad (24)$$

•) *The hydrostatic balance*

$$\nabla \left(\frac{1}{2} g h^2 \right) = -g h \nabla Z,$$

we prove from the hydrostatic balance that the model of the projected speed preserves the stationary state of the lake at rest

•) *The projected speed model*

$$\partial_t \begin{pmatrix} h \\ 0 \\ 0 \end{pmatrix} + 0 \times \partial_\eta \begin{pmatrix} h \\ 0 \\ 0 \end{pmatrix} = \begin{pmatrix} 0 \\ -g \partial_\eta (h + Z) \\ 0 \end{pmatrix}, \quad (25)$$

$$\partial_t h = 0, \quad \text{and} \quad \partial_\eta (h + Z) = 0 \implies h(x, y, t) + Z(x, y) = cst \quad \forall x, y, t.$$

This result ensures the equilibrium property corresponding to the lake at rest, and therefore it is consistent with the continuous form of the system's equilibrium with bathymetry source term.

$$\frac{\Delta t}{|T_i|} \sum_{j \in N(i)} |\gamma_{ij}| \Phi(W_{ij}^n, \mathbf{n}_{ij}) = \frac{\Delta t}{|T_i|} \int_{T_i} S dV, \quad (26)$$

which is equivalent to

$$\begin{pmatrix} 0 \\ \sum_{j \in N(i)} \frac{1}{2} g (h_{ij})^2 (n_{ij})_x |\gamma_{ij}| \\ \sum_{j \in N(i)} \frac{1}{2} g (h_{ij})^2 (n_{ij})_y |\gamma_{ij}| \end{pmatrix} = \begin{pmatrix} 0 \\ -g \int_{T_i} h \partial_x Z dV \\ -g \int_{T_i} h \partial_y Z dV \end{pmatrix}. \quad (27)$$

To approximate the source terms, we proceed as follows. First, we decompose the triangle T_i into three sub-triangles, as depicted in Fig.7.

where $N_{xij} = (n_{ij})_x |\gamma_{ij}|$, and $N_{yij} = (n_{ij})_y |\gamma_{ij}|$. Then, the source term is approximated as

$$\int_{T_i} h \partial_x Z dV = h_1 \int_{T_1} \partial_x Z dV + h_2 \int_{T_2} \partial_x Z dV + h_3 \int_{T_3} \partial_x Z dV, \quad (28)$$

with h_1, h_2 and h_3 are the average values of h over T_1, T_2 and T_3 respectively.

$$\begin{aligned} h_1 \int_{T_1} \partial_x Z dV &= \sum_{j \in N(1)} \int_{\gamma_{1j}} Z n_{xj} dV \\ &= h_1 \sum_{j \in N(1)} \frac{Z_1 + Z_j}{2} N_{x1j} \\ &= \frac{h_1}{2} \{ (Z_1 + Z_l) N_{x1l} + (Z_1 + Z_2) N_{x12} + (Z_1 + Z_3) N_{x13} \}. \end{aligned} \quad (29)$$

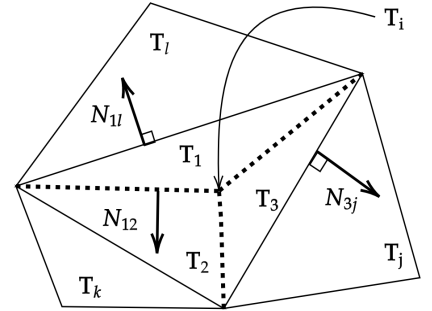


Fig. 7. Sub-triangles used in the discretization of source terms

The same applies to the y-direction.

Again the stationary flow condition $h_1 + Z_1 = h_j + Z_j = H = cst, \forall j \in N(1) \implies h_1 + h_j + Z_1 + Z_j = 2H$ and $H - \frac{h_1 + h_j}{2} = \frac{Z_1 + Z_j}{2}$. Thus, (29) gives

$$\int_{T_1} h \partial_x Z dV = h_1 \sum_{j \in N(1)} \left(H - \frac{h_1 + h_j}{2} \right) N_{x1j} \underbrace{\sum_{j \in N(1)} N_{x1j}}_{=0} = -\frac{h_1}{2} \sum_{j \in N(1)} h_j N_{x1j}.$$

Finally,

$$\int_{T_1} \partial_x Z dV = -\frac{h_1}{2} (h_l N_{x1l} + h_2 N_{x12} + h_3 N_{x13}).$$

A similar procedure leads to the following approximations of the other terms in (28)

$$\int_{T_2} \partial_x Z dV = -\frac{h_2}{2} (h_k N_{x2k} + h_1 N_{x21} + h_3 N_{x23}),$$

$$\int_{T_3} \partial_x Z dV = -\frac{h_3}{2} (h_j N_{x3j} + h_1 N_{x31} + h_2 N_{x32}).$$

Notice that h_l, h_k and h_j are the average values of h , respectively, on the triangle T_l, T_k and T_j . Summing up, using the fact that $(N_{xij} = -N_{xji})$ so, the discretization (28) gives

$$\int_{T_i} h \partial_x Z dV = -\frac{1}{2} (h_1 h_l N_{x1l} + h_2 h_k N_{x2k} + h_3 h_j N_{x3j}). \quad (30)$$

For this reconstruction, the source terms in (27) result in

$$\begin{aligned} \sum_{j \in N(i)} (h_{ij}^n)^2 N_{xij} &= h_1 h_l N_{x1l} + h_2 h_k N_{x2k} + h_3 h_j N_{x3j}, \\ \sum_{j \in N(i)} (h_{ij}^n)^2 N_{yij} &= h_1 h_l N_{y1l} + h_2 h_k N_{y2k} + h_3 h_j N_{y3j}. \end{aligned} \quad (31)$$

If you have noticed, we will need h_1, h_2 and h_3 to be able to calculate the values of the integrals in equation (30) but the system (31) has two equations for the three unknowns. To complete the system, we add the natural conservation equation, $h_1 + h_2 + h_3 = 3h_i$. The following system gives us the values we need

$$\begin{pmatrix} h_1 \\ h_2 \\ h_3 \end{pmatrix} = \begin{pmatrix} 1 & 1 & 1 \\ h_l N_{x1l} & h_k N_{x2k} & h_j N_{x3j} \\ h_l N_{y1l} & h_k N_{y2k} & h_j N_{y3j} \end{pmatrix}^{-1} \cdot \begin{pmatrix} 3h_i \\ \sum_{j \in N(i)} (h_{ij}^n)^2 N_{xij} \\ \sum_{j \in N(i)} (h_{ij}^n)^2 N_{yij} \end{pmatrix}. \quad (32)$$

Analogously, the bottom values Z_j , $j = 1, 2, 3$ are reconstructed in each sub-triangle of T_i as

$$\begin{cases} Z_1 = Z_i + h_i^n - h_1^n, \\ Z_2 = Z_i + h_i^n - h_2^n, \\ Z_3 = Z_i + h_i^n - h_3^n. \end{cases}$$

Finally the source terms in (30) are approximated as

$$\int_{T_i} h \partial_x Z dV = h_1 \sum_{m \in N(1)} \frac{Z_1 - Z_m}{2} N_{x1m} + h_2 \sum_{m \in N(2)} \frac{Z_2 - Z_m}{2} N_{x2m} + h_3 \sum_{m \in N(3)} \frac{Z_3 - Z_m}{2} N_{x3m}, \quad (33)$$

with a similar equation for the other source terms in the y-direction.

•) *Computation of the solution*

Finally, we write the formally well-balanced FVC scheme after calculation of the interface values (23) and the bathymetry source term approximation (33) as

$$W_i^{n+1} = W_i^n - \frac{\Delta t}{|T_i|} \sum_{j \in N(i)} |\gamma_{ij}| \Phi(W_{ij}^n, \mathbf{n}_{ij}) + \Delta t S_i^n. \quad (34)$$

3.2.5 Semi implied treatment of friction term source

To avoid stability problems related to the bottom friction source term, a fractional semi implied treatment for this term is proposed. The idea is to evaluate the momentum in the system (3) by decomposing it into two equations

$$\begin{cases} \frac{\partial h\mathbf{u}}{\partial t} = -\eta^2 g h^{-1/3} |\mathbf{u}| \mathbf{u} \\ \frac{\partial h\mathbf{u}}{\partial t} + \Phi_{h\mathbf{u}}(W) = -gh \nabla Z, \end{cases} \quad (35)$$

where $\Phi_{h\mathbf{u}}(W)$ represents the convection terms corresponding to the equations of the momentum. In a first step, a linearized semi implied method is used to integrate the first equation of the system (35)

$$\frac{(\tilde{h}\mathbf{u})_i - (h\mathbf{u})_i^n}{\Delta t} = -\eta^2 g (\tilde{h}\mathbf{u})_i |\mathbf{u}_i^n| (h_i^n)^{-4/3}. \quad (36)$$

In the second step, the value $(\tilde{h}\mathbf{u})_i$ is taken as the initial condition for solving the second equation of (35).

4 Numerical tests

It is clear from (23) that the scheme is conservative and can compute the numerical flux corresponding to the physical solutions of water flow without relying on Riemann problem solvers. The CFL condition for the explicit scheme (22) can be written

$$\Delta t \leq \min \left\{ \frac{|T_i|}{|\gamma_{ij}|(\mathbf{u} \cdot \mathbf{n} + \sqrt{gh})}, \frac{|T_i|}{|\gamma_{ij}|(\mathbf{u} \cdot \mathbf{n} + \sqrt{gh})\sqrt{2\alpha}}, \frac{|\gamma_{ij}|}{(\mathbf{u} \cdot \mathbf{n} + \sqrt{gh})\alpha} \right\}.$$

A fixed CFL = 0.9 is used and $\alpha = 2$ if not specified in the test. The used computer is an Intel Core i7-8565U CPU @ 1.80GHz \times 8, with 15 GB RAM.

In order to validate our FVC scheme on unstructured meshes to simulate shallow water flows, therefore we present some test cases that are proposed by several authors to validate their model and their numerical approach. The accuracy is demonstrated by comparing numerical solutions produced by the FVC scheme with analytical solutions, especially in tests 4.1, 4.2 and 4.3. To reproduce the calculation results reported in the literature, the source term of the bed is always taken into account. The C-property produced by this term has also been treated in tests 4.4 and 4.5. The Coriolis effect was taken into account in test 4.6 and this test's results are in good agreement with those presented in the literature. The test 4.7 compares the experimental data of a dam break flow in a channel with a 90° bend. This experiment was carried out in the laboratory of the Civil Engineering Department of the UCLouvain University, Belgium. We took into account the friction source term for this last simulation.

4.1 Accuracy test example

We test our approach on a problem where the exact solution is known [31]. It can be readily checked that.

$$h(t, x, y) = 1 - \frac{a^2}{4bg} \exp(-2b(\bar{x}^2 + \bar{y}^2)),$$

$$u(t, x, y) = M \cos(\theta) + a\bar{y} \exp(-b(\bar{x}^2 + \bar{y}^2)), \quad v(t, x, y) = M \sin(\theta) - a\bar{x} \exp(-b(\bar{x}^2 + \bar{y}^2)),$$

where, $\bar{x} = x - x_0 - Mt \cos(\theta)$ and $\bar{y} = y - y_0 - Mt \sin(\theta)$,

gives a smooth solution of the shallow water system (1) without the source terms (i.e. $\nabla Z = 0$, and $f_c = 0$) for any choice of constants, M, a, b, x_0, y_0 and θ . Initial and boundary condition are set according to the exact solution.

We let $M = \frac{1}{2}$, $g = 1$, $a = 0.04$, $b = 0.02$, and $(x_0, y_0) = (-20, -10)$. To test the scheme ability to resolve flows that are not aligned with the computational mesh, we let $\theta = \frac{\pi}{6}$. We compute for $(x, y) \in \Omega = [-50, 50] \times [-50, 50]$ up to time $t = 100$ s to compare the accuracy of our FVC scheme to the SRNH scheme originally introduced in [32, 33]. We also propose to see the effect of the choice of the parameter α . In [15] where the authors defined for the first time the FVC scheme in its one-dimensional formulation, were able to show that the parameter α controls the accuracy of the FVC scheme, for more rigorous details we invite you to see the Lemma 3.2 and its proof. Our study reaches the same conclusion on alpha as in Fig.9 we show the convergence order for three different choices of α .

Table 1: Relative L^1 errors and CPU times obtained for the accuracy test example at time $t = 100$ using the SRNH and FVC schemes.

Schemes	SRNH				FVC $_{\alpha=1}$			
	L^1 error			CPU time (s)	L^1 error			CPU time (s)
# Cells	h	hu	hv		h	hu	hv	
2648	2.042E-04	5.344E-03	9.546E-04	16.71	1.785E-04	4.379E-03	8.763E-03	11.91
10362	1.627E-04	7.626E-03	7.626E-03	31.30	1.078E-04	1.534E-03	3.475E-03	21.49
40690	1.317E-04	2.716E-03	5.450E-03	184.81	4.518E-05	5.430E-04	1.249E-03	101.46
161316	9.363E-05	1.628E-03	3.441E-03	1887.89	1.986E-05	2.083E-04	4.868E-04	1003.26
640138	8.526E-05	9.871E-04	1.067E-03	21031.82	1.066E-05	1.771E-04	3.278E-04	10524.03

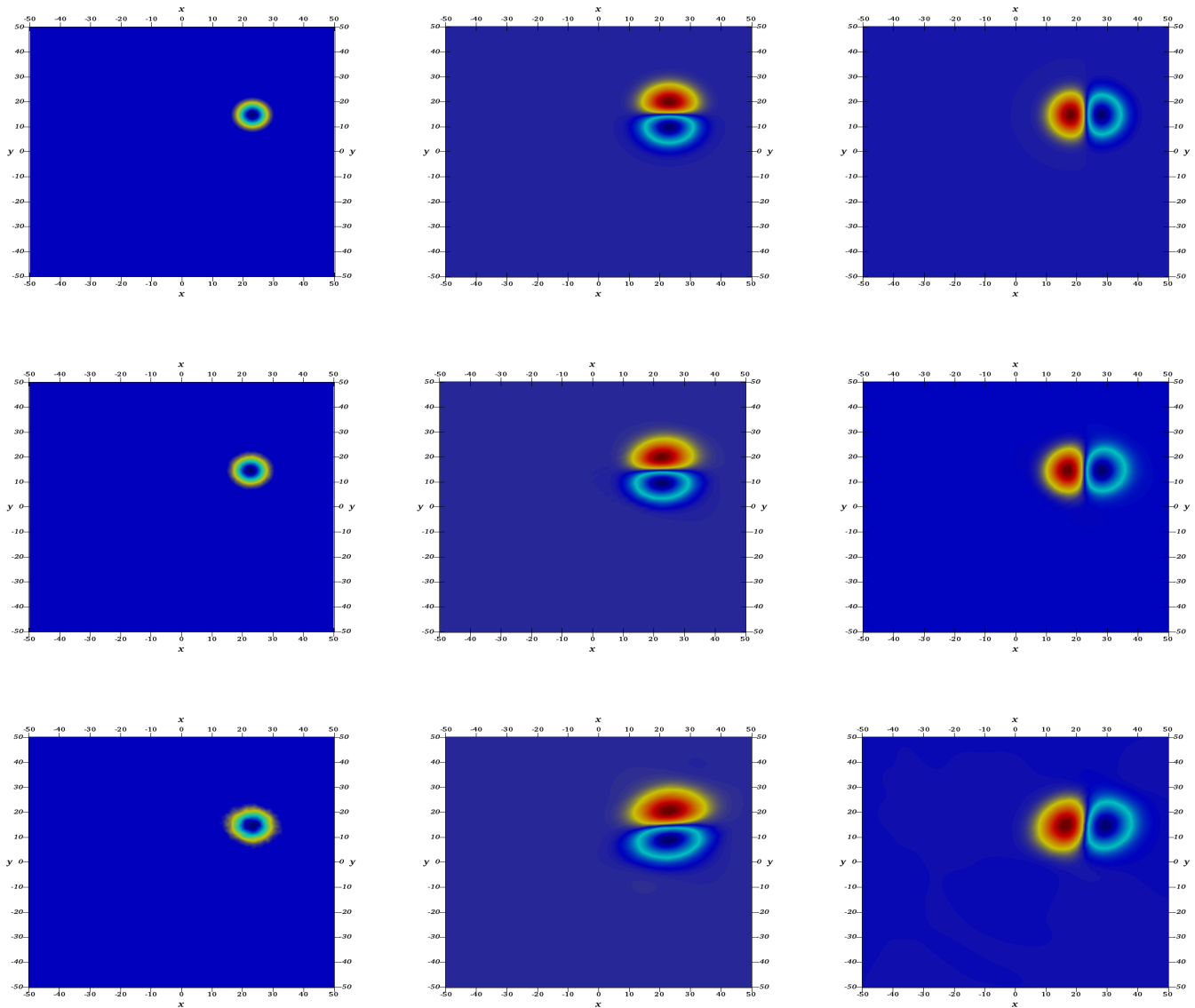


Fig. 8. Water depth h and discharge hu and hv for the accuracy test example. First row: Exact solution. Second row: FVC scheme. Third row: SRNH scheme using a mesh with 10362 cells at $t = 100$ s.

The results in Table 1 show that increasing the number of the cells in the computational domain lead to a decrease in the L^1 error for the water height h , and the discharges hu and hv in all schemes. Faster decay of the error is observed in the FVC scheme than in the SRNH scheme which is only natural a simple inspection of Table 1 also reveals that for meshes with a low number of the cells, the measured computation time is comparable for the SRNH scheme and FVC scheme. However, for meshes with a somewhat large number of cells, the FVC method is the most efficient. For example, a mesh of 161316 cells, the FVC scheme is about two faster than the SRNH scheme this is due to our FVC approach is not based on the calculation of the Jacobian matrix of the system, this matrix intervenes in many Q-scheme type approximation schemes, it is responsible for the slowness of this kind of scheme. Note that the SRNH scheme requires a solver for the Riemann problem at each time step to reconstruct the numerical flux, which is completely avoided in our FVC scheme. We can see that both schemes could reach the designed order of accuracy. In Fig.9 we have plotted the log of L^1 error calculated in Table 1 and the other values calculated for $\alpha = 0.5$ and then $\alpha = 2$ against the log of the maximum value of the mesh edges. We find that the L^1 errors of the FVC scheme lie on a slope line 1.4, indicating that the accuracy order of the scheme is about 1.4 for $\alpha = 0.5$.

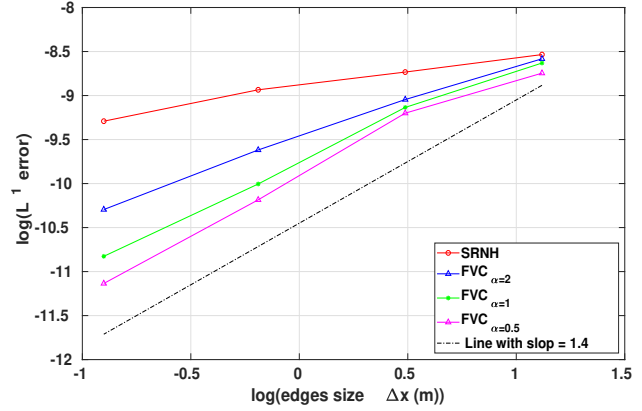


Fig. 9. Convergence order in L^1 error of a water height.

4.2 Dam-break problem

Flood flows produced by the dam break, segments of dykes, or other structures are torrential in nature with the presence of a discontinuous front propagating downstream and a rarefaction wave propagating upstream. The characteristics of these flows such as velocity, water level and time of arrival of floods must be determined in advance in order to manage floods and reduce their impact on the environment and economic infrastructure. In order to test our approach for problems related to dam break, we carried out a series of test cases proposed in the literature (see, e.g. [15, 34, 35]) etc. The proposed approach is not based on a Riemann solver technique which is very appropriate for a hyperbolic problem whose solution is often represented by a discontinuous front. Thus it will be interesting to examine the accuracy of our approach by simulating torrential flows with the presence of a discontinuity in the velocity profile and the free surface.

•) Description of the problem

We consider a rectangular channel with a flat bottom, $Z(x, y) = 0$ and no friction, i.e. there is no source terms, the problem is purely hyperbolic. The channel is 1.6 m long and 0.1 m wide (we assume a nondimensionalization problem), the initial conditions are given by

$$h(0, x, y) = \begin{cases} h_l & \text{if } x \leq x_m, \\ h_r & \text{if } x > x_m, \end{cases} \quad 0 \leq y \leq 0.1$$

$u(0, x, y) = v(0, x, y) = 0$ m/s. A dam is placed in the middle of the channel i.e. $x_m = 0.8m$

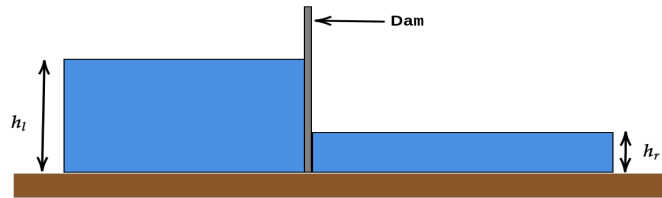


Fig. 10. Initial condition of the problem.

This corresponds to a homogeneous Riemann problem. Initially, the water is at rest, the height h_l remains 1.0 m for all simulations. The downstream height h_r takes on different values 0.5 m, 0.1 m, and 0.025 m. The nature of the torrential flow due to the dam break depends essentially on the ratio h_r/h_l .

A numerical instability is likely to occur for small values of the ratio h_r/h_l . At $t = 0$, it is assumed that the dam is abruptly removed causing a shock wave with the presence of a discontinuous front of the water surface propagating downstream. The channel is assumed to be closed on all four sides and the "slip" conditions is imposed on all walls. The computational domain is discretised by a mesh of 41776 triangles with an average size of $0.003m^2$. We will compare the water height and velocity obtained by our approach with the analytical solution which is calculated using the Stoker method [36], its expression is written in the Appendix.

The evolution of the water surface profile is used to examine the behaviour of the FVC scheme in capturing the discontinuous shock front. Henderson [37] notes that when the ratio h_r/h_l is greater than 0.138, the flow is sub-critical in the whole of the channel. When the ratio h_r/h_l is smaller than 0.138, the flow is supercritical downstream and sub-critical upstream of the dam. For very small values of h_r/h_l , the upstream flow regime becomes strongly supercritical, and it may be difficult to capture such a shock wave numerically.

•) *Results and discussion*

The first simulation concerns a river flow with $h_r/h_l = 0.5$. The Fig.11 shows the cross-section at $y = 0.05$ of the evolution of the water depth and the longitudinal velocity. Excellent agreement is obtained between the numerical and analytical results, this is clear from Table 2 where the L^1 error and the accuracy order of h and hu are presented respectively. The comparison shows that, under this condition, our scheme, can accurately predict the shock wave without creating oscillations.

In [38] the authors have proven that for a ratio h_r/h_l smaller than 0.05, most of the existing numerical models cannot give accurate results especially on the front. The last simulations, with $h_r/h_l = 0.1$ and 0.025 (see Fig. 12 and Fig.13), create supercritical flows downstream and sub-critical flows upstream. When $h_r/h_l \leq 0.025$, a slight, non-physical oscillation occurs at the shock front.

Table 2: Relative L^1 error and CPU times for dam break test at $t = 0.1$ s using FVC scheme on a different meshes.

# Cells	Maximum of edges size	Error in h	Error in hu	Ordre	CPU time (s)
5252	0.0127	2.612E-03	2.189E-02	-	7.91
10632	0.00913	1.650E-03	1.378E-02	1.402	10.66
21224	0.00666	1.045E-03	8.711E-03	1.453	19.96
41776	0.00479	6.255E-04	5.169E-03	1.583	30.21

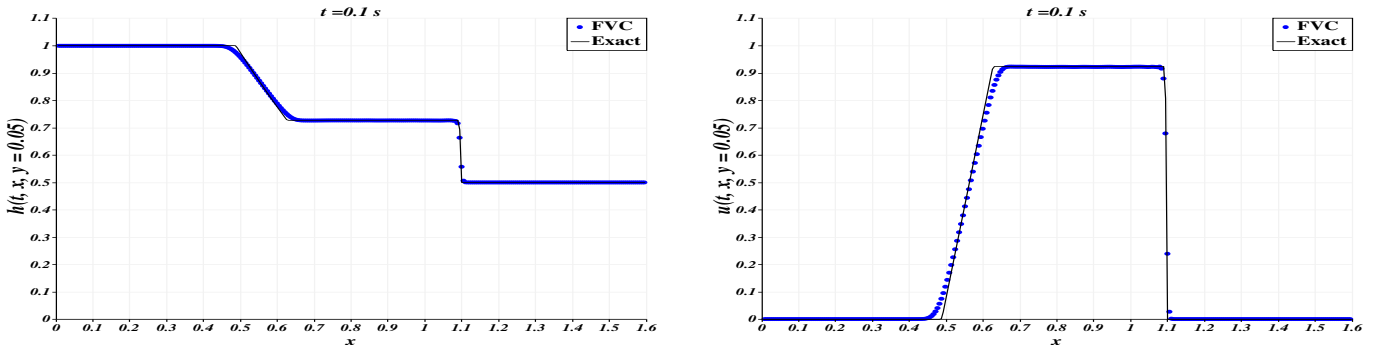


Fig. 11. Comparison of results for $h_r/h_l = 0.5$ at $t = 0.1$ s. Left: water height h . right: longitudinal velocity u .

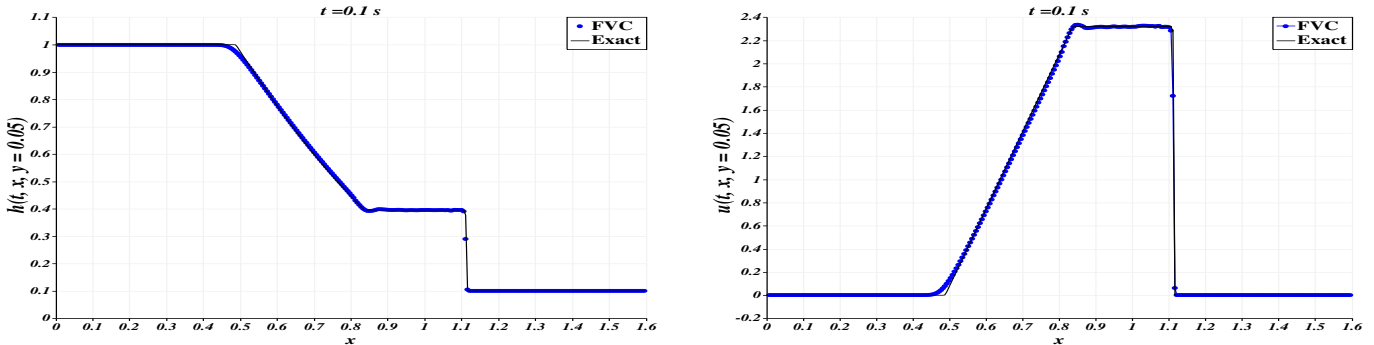


Fig. 12. Comparison of results for $h_r/h_l = 0.1$ at $t = 0.1$ s. Left: water height h . right: longitudinal velocity u .

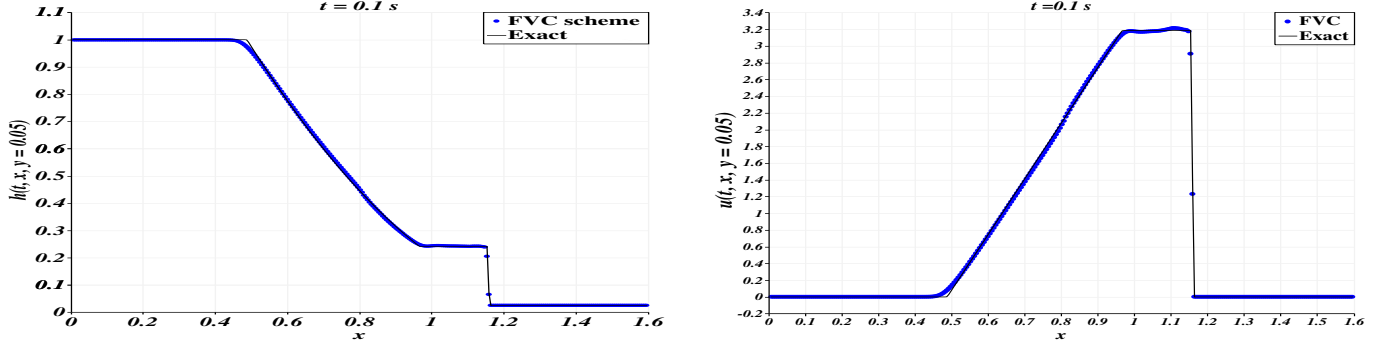


Fig. 13. Comparison of results for $h_r/h_l = 0.025$ at $t = 0.1$ s. Left: water height h . right: longitudinal velocity u .

The ratio h_r/h_l is largely responsible for the problem of numerical instabilities that occur in the simulation of torrential flow due to dam failure. The difficulty of the problem increases with the decrease of the ratio h_r/h_l . We conclude that the proposed approach is well able to simulate torrential flows with a good capture of the shock front for the ratio h_r/h_l very small.

The previous test case was one-dimensional in nature. In the real applications, torrential flows due to dam and dike segment failure are often two-dimensional. Therefore, the objective of the Fig.14 is to show you the ability of the proposed scheme to reproduce two-dimensional flood propagation in the presence of a discontinuous front of water height and velocity over a wet bottom. This problem has been treated by many authors to validate their dam break models approximation schemes (see . e.g. [39, 40]).

We supposed that at $t = 0$, abruptly reservoir dam is partially broken and unsymmetrical over a length of $75m$. Initially $h_r/h_l = 0.5$ is fixed with $h_l = 10m$ as water depth in the reservoir and $h_r = 5m$ as the water level downstream of the dam. The water in the basin is at rest at $t = 0$, that is $u(0, x, y) = v(0, x, y) = 0m/s$. The gravitational acceleration is fixed to $g = 9.81m/s^2$ and the duration of simulation is 7.2 s counted from the partial dam break.

The figures Fig.14, Fig.15 left and right, show the results of the height in three-dimensional view, the gradient contour of the water height as well as the corresponding velocity field respectively at physical time 7.2 s. We have used a mesh of 4066 non-uniform triangles as you can see in the Fig.14.

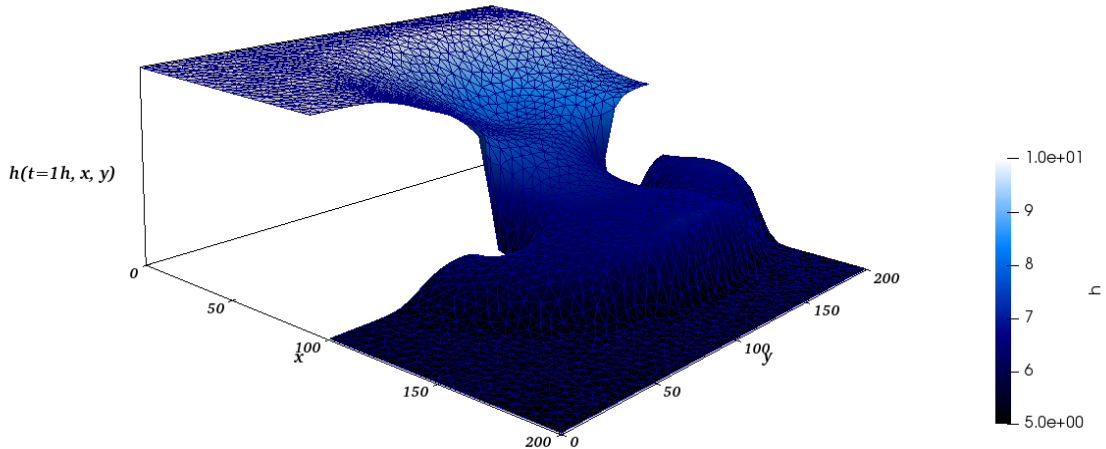


Fig. 14. Water height at $t = 7.2$ s.

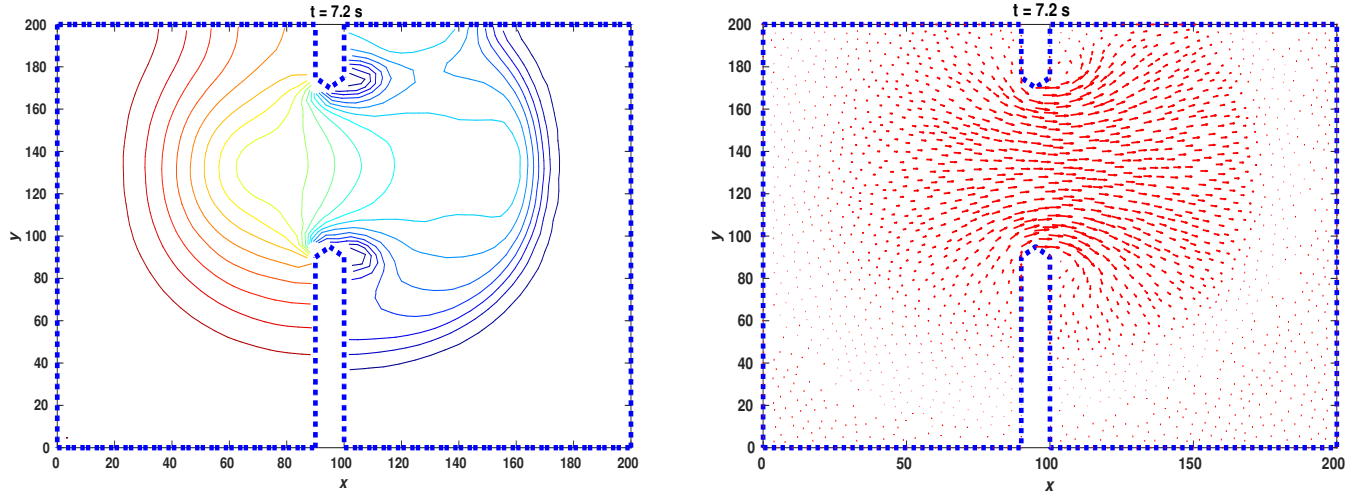


Fig. 15. left: gradient contour & right: velocity vector field.

We can observe that the right-hand flow propagates downstream from top to bottom, the rarefaction wave propagates upstream and two asymmetric weak eddies develop on both sides of the rift. Good resolution is obtained in regions with steep water level gradients, such as moving fronts. Furthermore, the global flow is preserved without excess numerical diffusion. Our results seem to be very similar to those presented by the existing studies mentioned above.

In order to show the convergence accuracy of our approach the same simulations were performed on three types of meshes: mesh 1 is a coarse mesh with 2012 triangles, mesh 2 has twice the number of the mesh 1 triangles, 4066 triangles and a fine mesh with 10083 triangles. A reference solution is also used to quantify the numerical results obtained on the three meshes. In Fig.16, we present the cross-sections of the water height and the hu discharge in different meshes along the axes $y = 125m$ at time $t = 7.2s$.

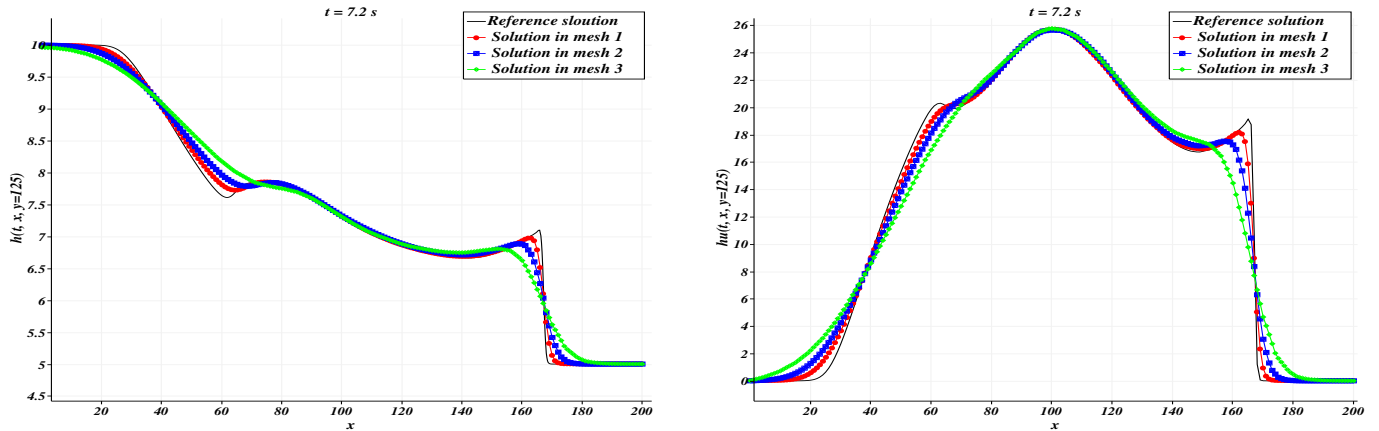


Fig. 16. Horizontal cross-sections at $y = 125m$ of the water depth (left Fig) and the water velocity (right Fig) for the partial dam-break problem obtained by using different meshes at time $7.2s$.

This test case confirms the ability of the scheme to reproduce two-dimensional flows in the presence of a discontinuous front. The uncovering and overlapping domains are well treated by the scheme. Furthermore, this test case allows us to perform the calculations using our approach to determine both the water head and the velocity at the open boundary. It excludes numerical oscillations, therefore it is stable.

4.3 Tidal wave flow over an irregular bed

Here we propose to study a tidal flow on a very irregular bed. This test case has been proposed in several works to validate and to test the C-property of their approximation method [41, 5]. So this test example is a good illustration of the significance of the source term treatment for practical applications to natural watercourses. It is well known that in the shallow water equations describing a flow over a very irregular background, the source terms become dominant and may cause undesirable numerical instabilities. Therefore this test case allows us to test the reliability and robustness of the proposed model when the bottom variation is fast and irregular. The bed topography is defined in Appendix (Table of bed elevation $Z(x)$ and its illustration). The initial and boundary conditions are constructed from the asymptotic analytical solution is given by

$$h(t, x) = h_0 + 4 - Z(x) - 4 \sin\left(\pi\left(\frac{4t}{86400} + \frac{1}{2}\right)\right), \quad u(t, x) = \frac{\pi(x - 1500)}{5400 \cdot h(t, x)} \cos\left(\pi\left(\frac{4t}{86400} + \frac{1}{2}\right)\right)$$

but with, $h_0 = 16 \text{ m}$, $h(0, x) = h_0 - Z(x)$.

In order to compare the numerical results of our approach with the analytical solution, we choose two results, at $t = 10800 \text{ s}$ and at $t = 32400 \text{ s}$. In Fig.17 we present a comparison between the approach surface level and the analytical solution at $t = 10800 \text{ s}$ as well as the water height at the same time using a mesh of 200 grid points in x-direction. We also include in Fig.18 a comparison between the water velocity generated by the FVC scheme and the analytical velocity at $t = 10800 \text{ s}$ then at $t = 32400 \text{ s}$. In Table 3 we present a comparison between the exact solution and the solution generated by FVC scheme using the relative L^1 error. An excellent agreement is obtained between the numerical and analytical solutions. This confirms that the proposed scheme is also accurate for tidal flow over an irregular bed. Moreover, these results are qualitatively in good agreement with those published in [41, 5].

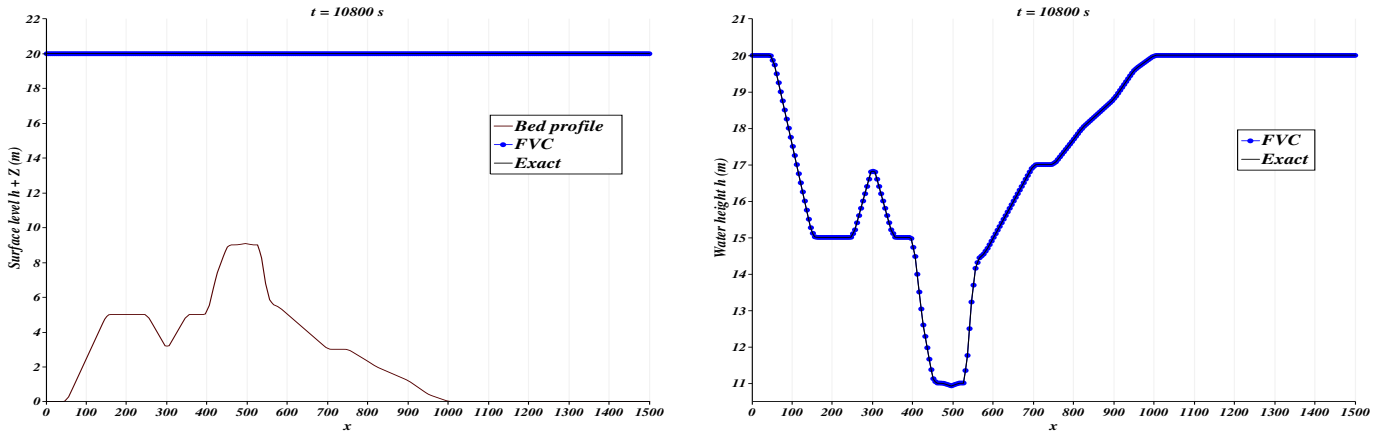


Fig. 17. Tidal wave flow over an irregular bed. Left: Comparison of surfaces level $h + Z$ at $t = 10800 \text{ s}$ and bed Z . Right: Comparison of water height h .

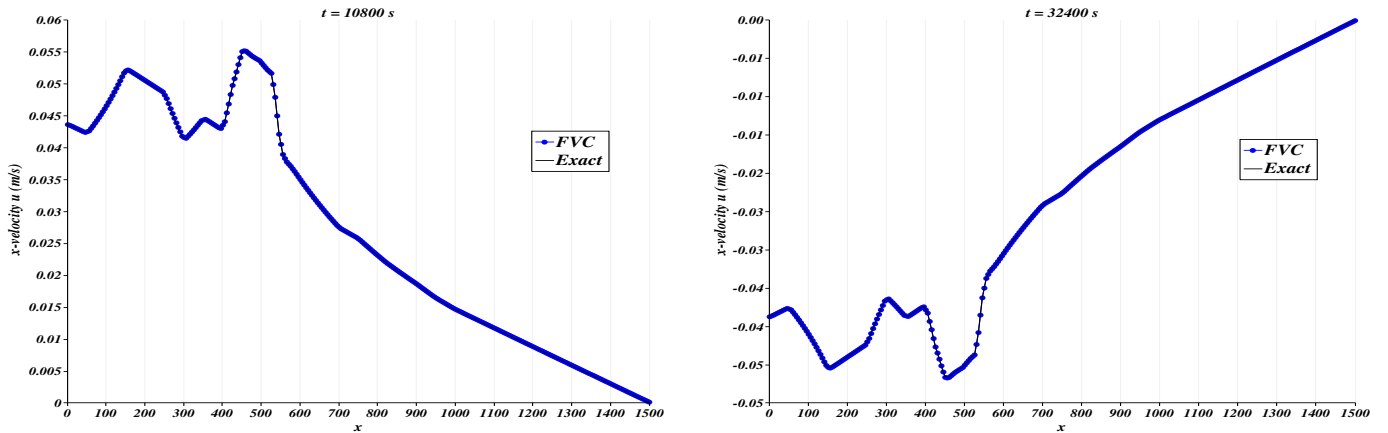


Fig. 18. Comparison of water velocity u in tidal wave flow over an irregular bed. Left: at $t = 10800 \text{ s}$. Right: at 32400 s .

The accuracy of the proposed scheme in the treatment of the source terms has been identified. The numerical errors produced by the model remain very low despite the fact that the mesh is coarse and the bed is very irregular. The results of this test case confirm the good performance of our approach in the treatment of the source terms, while avoiding undesirable numerical errors due to the rapid variation of the bed.

Table 3: Relative L^1 error and CPU times for the tidal wave flow over an irregular bed using FVC scheme.

t_{end}	Error in h	Error in hu	Error in $h + Z$	CPU time (s)
10800	1.254E-05	4.230E-03	1.012E-05	545.95
32400	7.719E-06	5.731E-03	1.241E-05	1583.41

4.4 Flow over a non-flat irregular bed

•) *Case 1*

We consider the example of water flow in a two-dimensional channel including an irregular bed, a similar test has been proposed in [5]. The mathematical formulation consists of solving the shallow water system (1) without Coriolis force and subjected to Neumann boundary conditions.

The initial conditions as follow

$$h(0, x, y) = 1 - Z(x, y) \text{ m}, \quad u(0, x, y) = v(0, x, y) = 0 \text{ m/s},$$

where the bed profile is defined by:
$$Z(x, y) = \sum_{k=1}^5 a_k \exp\left(-\frac{(x - x_k)^2 + (y - y_k)^2}{\sigma_k^2}\right),$$

with $(a_1, \sigma_1^2, x_1, y_1) = (0.75, 2, -4, 5)$, $(a_2, \sigma_2^2, x_2, y_2) = (0.7, 2, -2.5, 2.5)$, $(a_3, \sigma_3^2, x_3, y_3) = (0.65, 3.3, 0, 0)$, $(a_4, \sigma_4^2, x_4, y_4) = (0.6, 2.5, 3, -2)$, and $(a_5, \sigma_5^2, x_5, y_5) = (0.55, 1.48, 5, -4)$.

The purpose of this test example is to verify the achievement of the C-property for the FVC scheme applied to shallow water flows over non-flat bed.

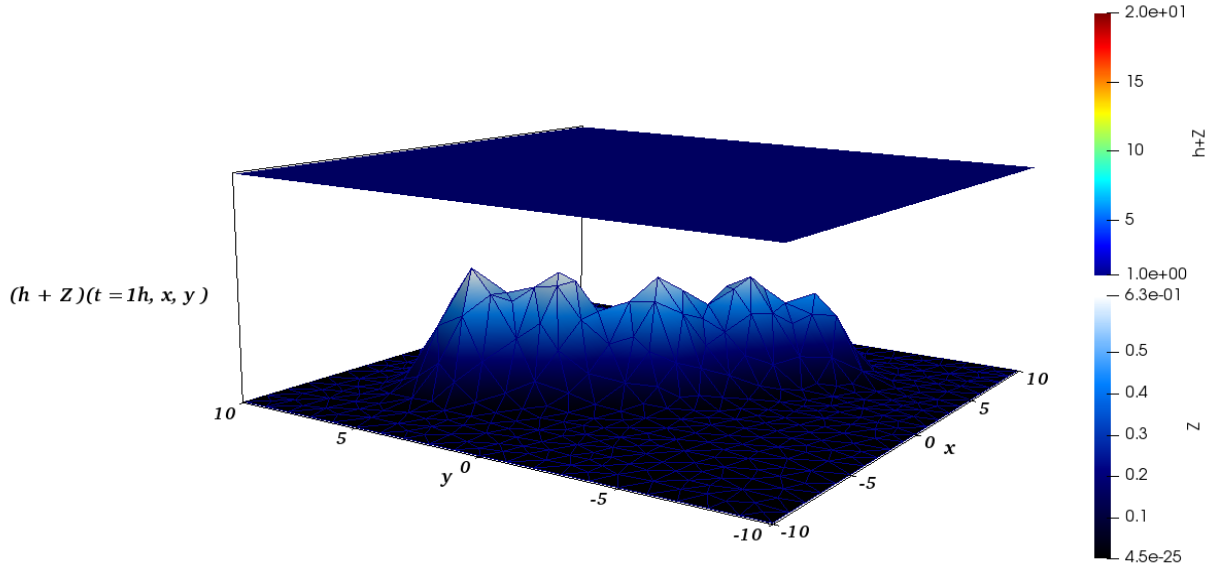


Fig. 19. Water free-surface for the flow over a non-flat irregular bed at $t = 1$ hour.

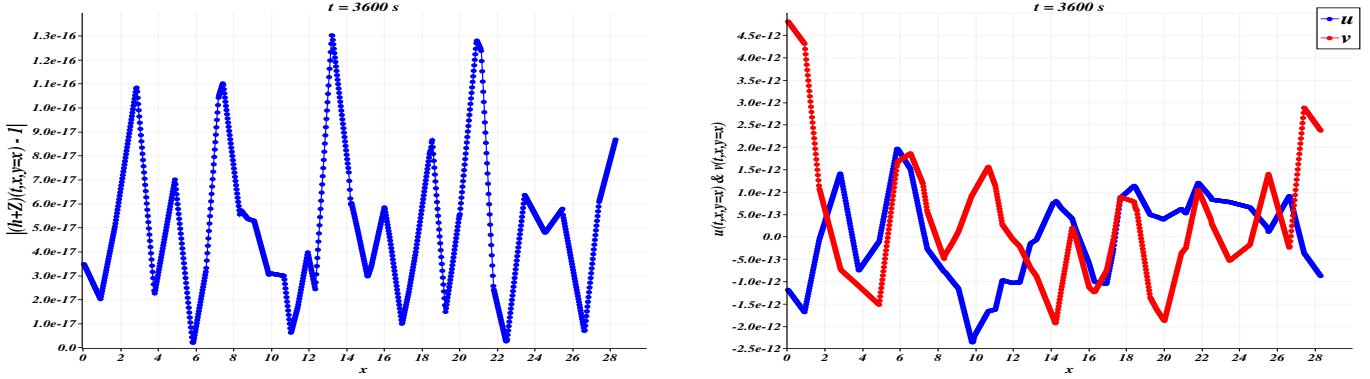


Fig. 20. Cross-sections at $y = x$. Left: the absolute error of the free-surface for the lake at rest. Right: velocities values after 1 hour.

The C-property of well-balanced FVC scheme on unstructured meshes is checked in this example. In Fig.19, we present the water free-surface obtained at time $t = 3600 s$ using an unstructured mesh of 1030 cells. As expected the water free-surface remains constant during the simulation time. The velocities and the error presented in Fig.20 also show that the equilibrium of the lake at rest is verified. All this shows that the proposed FVC scheme perfectly preserves the C-property.

•) *Case 2*

We will treat the same problem as case 1 but this time with a very large computational domain $\Omega = [0, 1500] \times [0, 500]$ and a non-smooth bed profile. As you have seen in case 1, the C-property is verified with a qualitatively admissible accuracy but the idea behind using this case is to compare the accuracy of our approach with the results of work that has been done using a Cartesian mesh (see subsection 4.1 of [16]).

The bed profile and the initial condition are defined as

$$h(0, x, y) = 20 - Z(x, y) \text{ m}, \quad u(0, x, y) = v(0, x, y) = 0 \text{ m/s}, \text{ the bed profile } Z(x) \text{ is defined in Appendix.}$$

The results presented in Table 4 and in the figures, Fig.21 and Fig.22 are in good agreement and even better than those in [16]. They also show that our approach preserves with good accuracy of the C-property regardless the complexity of the bed.

Table 4: L^1 and L^∞ errors of the water free surface for flow over a non-flat irregular bed case 2 at 1h, 2h then 3hours.

# Cells	Maximum of edges size	L^1 error			L^∞ error		
		$t = 3600s$	$t = 7200s$	$t = 10800s$	$t = 3600s$	$t = 7200s$	$t = 10800s$
776	68.94	1.700E-15	3.109E-15	3.231E-14	2.664E-15	4.085E-15	3.428E-14
1664	50.96	1.401E-15	3.023E-15	6.332E-15	1.580E-15	8.881E-16	8.015E-16
3218	35.58	4.845E-16	4.813E-16	7.011E-16	1.010E-15	8.881E-16	8.015E-16

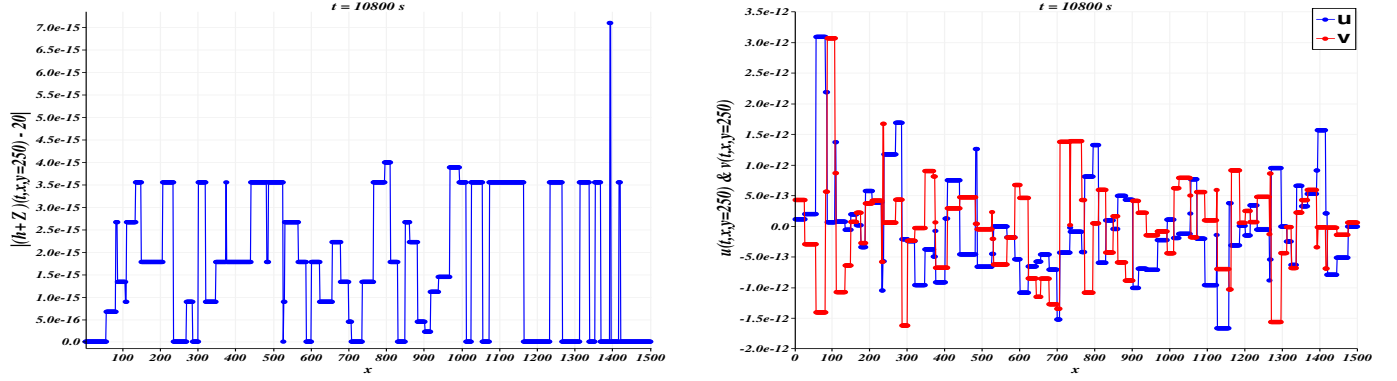


Fig. 21. Cross-sections at $y = 250$. Left: the absolute error of the free-surface for the lake at rest. Right: velocities values at 10800s.

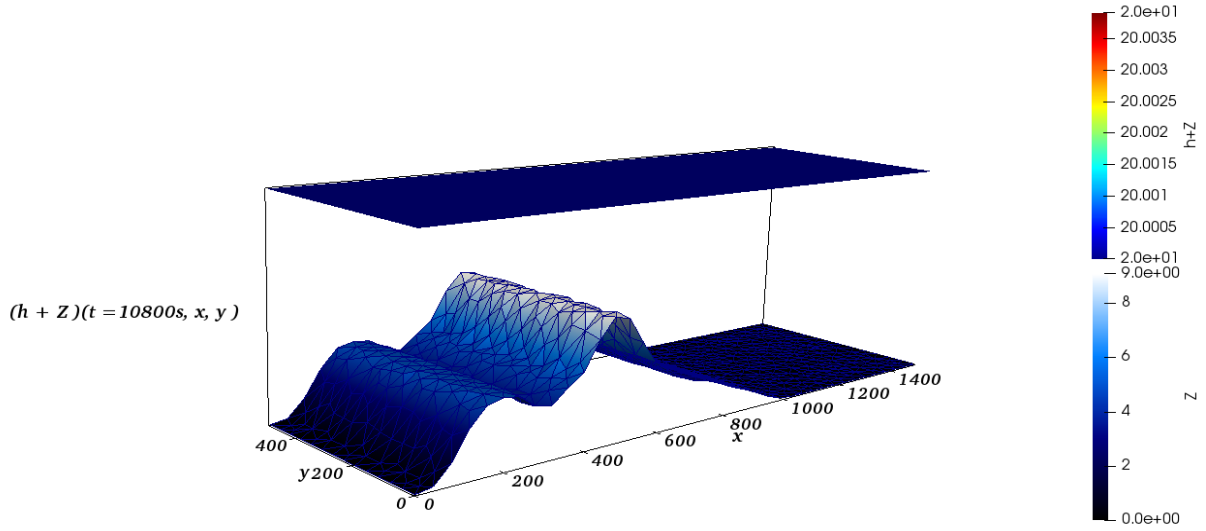


Fig. 22. Water free-surface for the flow over a non-flat irregular bed case 2 using a mesh with 1664 cells at $t = 10800$ s.

4.5 A small perturbation of a steady-state over a smooth bed

This test was introduced by R.J. LeVeque in [8] and recently used in [42]. This is a classical example to show the capability of the proposed well-balanced FVC scheme for the perturbation of the stationary state. We solve the two-dimensional shallow water equations in the rectangular domain $\Omega = [0, 2] \times [0, 1]$ subjected to Neumann boundary conditions and the following initial conditions

$$h(0, x, y) = \begin{cases} 1 - Z(x, y) + 0.01 & \text{if } 0.05 \leq x \leq 0.15, \\ 1 - Z(x, y) & \text{otherwise,} \end{cases} \quad 0 \leq y \leq 1, \quad u(0, x, y) = v(0, x, y) = 0 \text{ m/s.}$$

It is assumed that the bottom has the following form: $Z(x, y) = 0.8 \exp(-5(x - 0.9)^2 - 50(y - 0.5)^2)$.

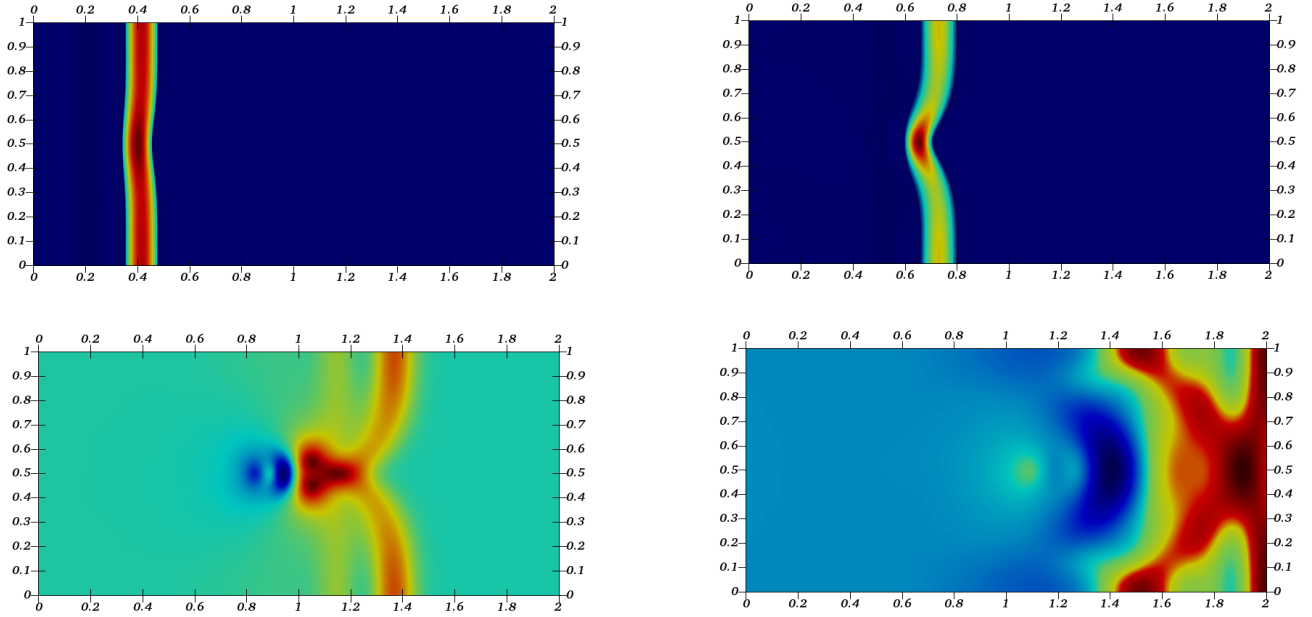


Fig. 23. Illustration of the surface level $h + Z$ at times $t = 0.10$ s, 0.20 s, 0.40 s, 0.60 s, respectively.

Fig.23 displays the right going disturbance as it propagates the hump on unstructured triangular mesh of 165008 cells, the surface level $h + Z$ are shown at different times. From top to bottom: $t = 0.10$ s from 0.999906 m to 1.003861 m; $t = 0.20$ s from 0.999733 m to 1.004363 m; $t = 0.40$ s from 0.998553 m to 1.001256 m; and $t = 0.60$ s from 0.999339 m to 1.000898 m. The results indicate that the FVC scheme can resolve the complex small detail of the flow over a smooth bed very well.

4.6 Circular dam-break problem

We consider the benchmark problem proposed in [43] to study cyclone/anticyclone asymmetry in nonlinear geostrophic adjustment. We solve the shallow water system (1) with a Coriolis effect on a non-flat bottom in the spatial domain $\Omega = [-10, 10] \times [-10, 10]$ subjected to Neumann boundary conditions and the following initial conditions

$$h(0, x, y) = 1 + \frac{1}{4} \left(1 - \tanh \left(\frac{\sqrt{ax^2 + by^2} - 1}{c} \right) \right), \quad u(0, x, y) = v(0, x, y) = 0 \text{ m/s},$$

where $a = \frac{5}{2}$, $b = \frac{2}{5}$, $c = 0.1$, $f_c = 1 \text{ Kg.m/s}^2$ and $g = 1 \text{ m/s}^2$.

The bottom profile has the following expression: $Z(x, y) = 0.3 \left(1 + \tanh \left(\frac{3x}{2} \right) \right)$.

Let's start by looking at the behaviour of this phenomenon in a domain with a flat bottom. The Fig.24 shows the representation of the water level calculated at different times for this test case with $Z(x, y) = 0$. As can be seen, a hole has formed and water is flowing out of the deepest region as a rarefaction wave progresses outwards. It is clear from the results presented that the initial elliptical mass imbalance evolves in a non-axisymmetric manner. The two expected shock waves are very well captured by the proposed FVC method. These results are qualitatively in good agreement with those published in [16, 43]. In Fig.25 we exhibit the results for the velocity field corresponding to the plots Fig.24. As can be seen the two shock waves originated behind the water elevation are slowly spinning clockwise in the computational domain. The velocity field is well represented by the FVC method and re-circulation regions within the flow domain are well captured.

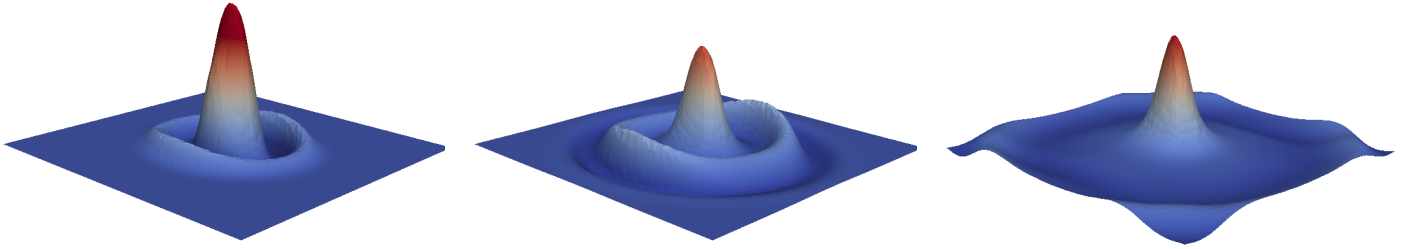


Fig. 24. Water depth for the circular dam-break problem on flat bottom obtained at different times using a mesh with 10040 cells. From top to bottom $t = 4$ s, 8 s and 16 s.

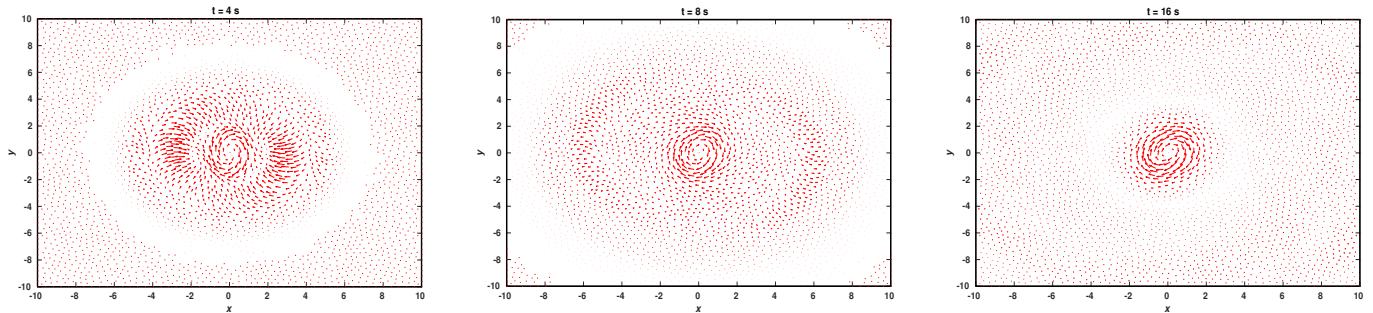


Fig. 25. Velocity fields for the circular dam-break problem corresponding to the plots represented in Fig.24.

Let's move on to the case of the non-flat bottom to assess the performance of our FVC scheme on unstructured meshes to solve the circular dam-break problem on a non-flat bottom. The Fig.26 shows the calculated results for the water depth at $t = 2$ s, 8 s and 16 s using two meshes of 10040 and 40146 cells. The corresponding results for velocity field are presented in Fig.27. From a numerical point of view this test example is more difficult than the previous one as the flow is expected to exhibit complex features due to the interaction between the water surface and the bed. As in the previous test a hole has formed and the water drains from the deepest region as a rarefaction wave progresses outwards. However, a slower propagation is detected for the water free-surface in this test compared to the simulations on flat-bottom.

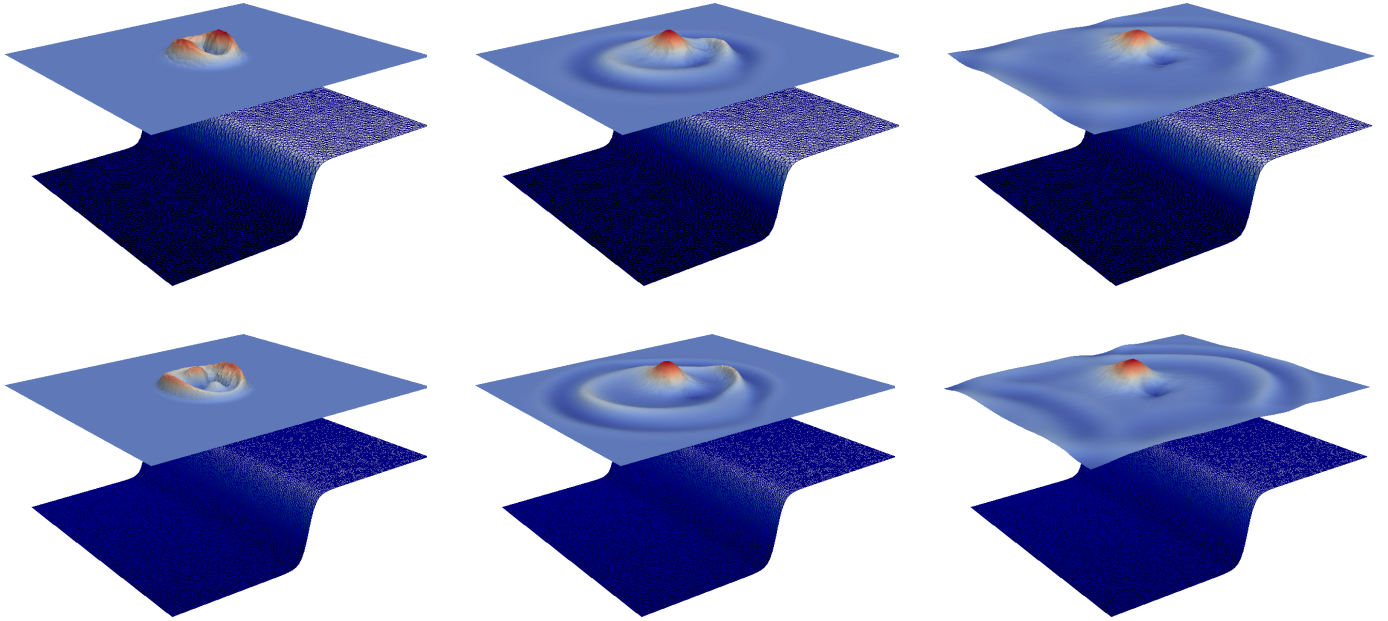


Fig. 26. Water depth for the circular dam-break problem on non-flat bottom obtained using a mesh with 10040 cells (first row) and 40146 (second row). From left to right $t = 2$ s, 8 s and 16 s.

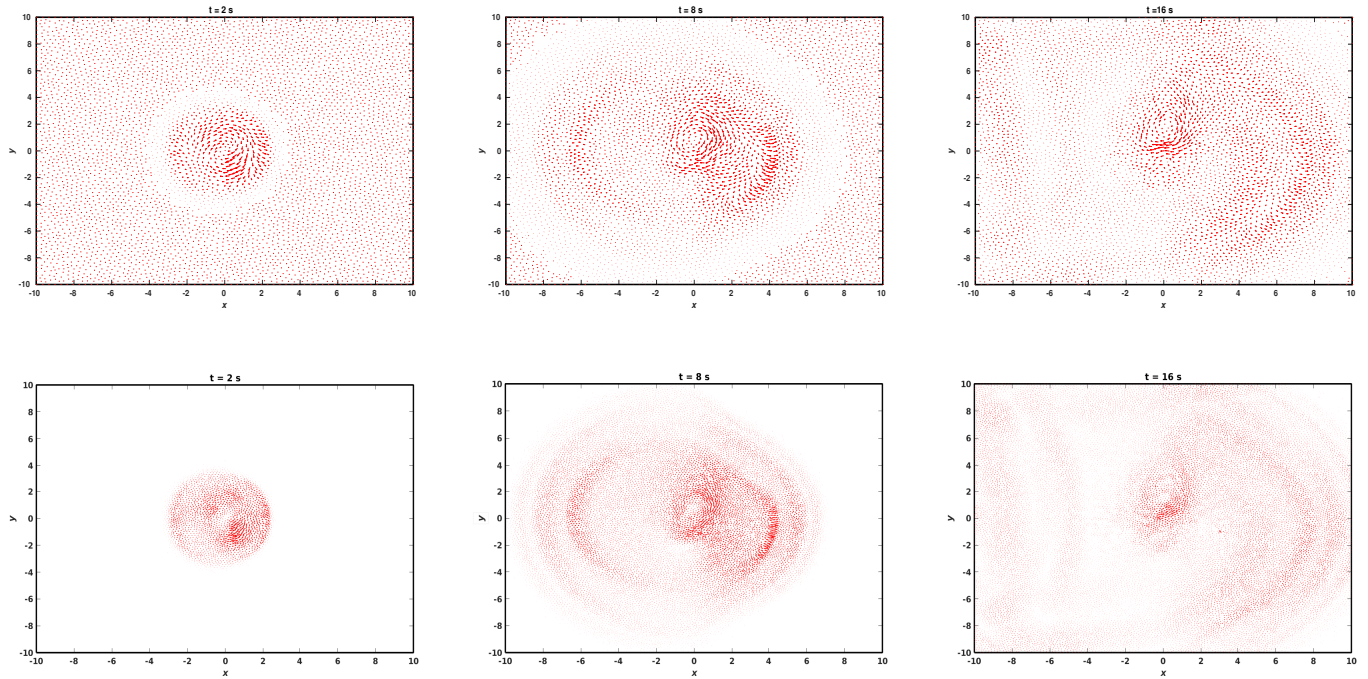


Fig. 27. Velocity fields corresponding to the plots represented in Fig.26. First row: mesh with 10040 cells. Second row: mesh with 40146 cells.

4.7 Tidal wave of a dam burst: Experimental validation

The previous test cases concern the simulation of different types of flows in non-complex geometries and without frictions. Under these conditions, we do not generally encounter numerical problems due to the complexity of the computational domain. The present test case is used to evaluate the ability of the proposed model to calculate the flows due to a dam break through a 90° bend on a

non-flat bottom with a large discontinuity in the bottom profile as well as the assumption of frictions terms. This is a physical experiment carried out in the framework of the European CADAM project in the laboratory of the Civil Engineering Department of the UCLouvain University, Belgium [44], for which a number of velocity and water level measurements are available in a laboratory channel.

•) *Description of the problem*

The geometry used in the experimental facilities consists of a square reservoir of $2.44 \text{ m} \times 2.39 \text{ m}$ and a 7.83 m long channel with a 90 bend as shown in Fig.28. The channel bed level is 0.33 m above ground level. The bed is relatively smooth with a Manning friction coefficient of $0.0095 \text{ s.m}^{-\frac{1}{3}}$. The initial water level in the reservoir is 0.25 m and 0.01 m in the whole channel. The authors of [45] used this test case to validate their numerical model which is based on the solution of the shallow water equations over complex topography with wetting and drying. In order to compare our approach with the experimental results we propose six measurement points which are located at G_1 ($1.19 \text{ m}, 1.21 \text{ m}$), G_2 ($2.74 \text{ m}, 0.69 \text{ m}$), G_3 ($4.24 \text{ m}, 0.69 \text{ m}$), G_4 ($5.74 \text{ m}, 0.69 \text{ m}$), G_5 ($6.56 \text{ m}, 1.51 \text{ m}$) and G_6 ($6.56 \text{ m}, 3.01 \text{ m}$), exactly like the study we cited above. These measurements allow us to illustrate and compare the output of our code with the results of the experiment. The computational domain is discretised by an unstructured triangular mesh of 6165 cells see Fig.29

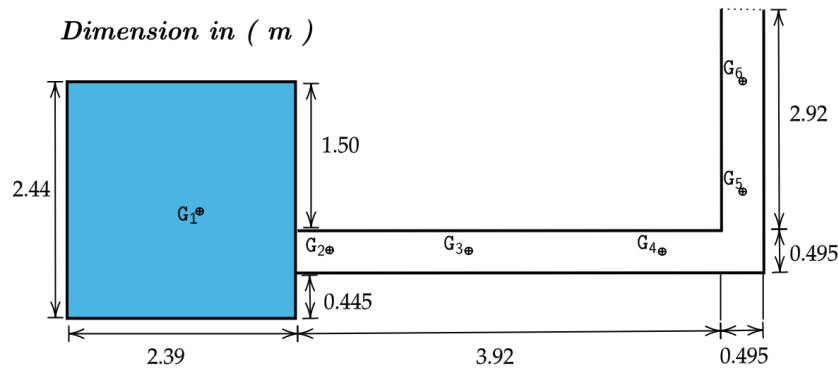


Fig. 28. Plane view of the reservoir and the channel, dimensions in (m).

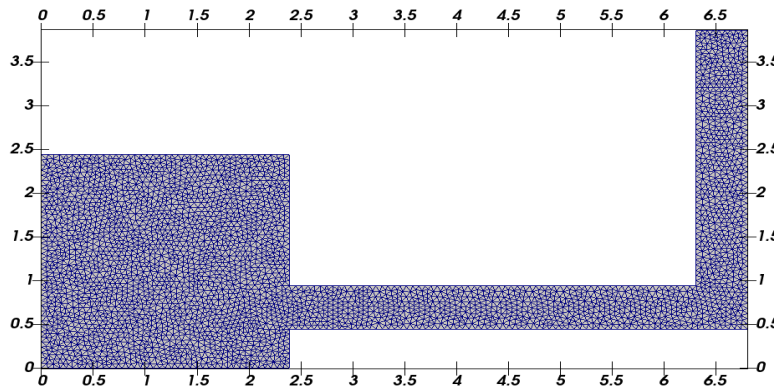


Fig. 29. Unstructured mesh of the computational domain.

•) *Results and discussion*

The Fig.30 present the free surface and bottom profile obtained by our simulation at $t = 3s, 5s, 7s,$ and $14s,$ respectively. These figures show that the supercritical flow induced by the rupture of the dam is reflected in the bend, its speed becomes zero and the water level rises. Then this column of water collapses and a new waterfront propagates both downstream and upstream. Upstream, this

results in a bore receding towards the reservoir, however the flow rate at the head of the bore is now subcritical, and therefore much slower than the initial supercritical flow. After this very transient phase, the flow approaches, stable conditions where the inclination of the free surface is close to the description presented by [44]. Fig.31 allows us to compare the water height h obtained by our scheme with the experimental measurements. Our scheme gives values of h almost identical to the measured values, especially in the critical areas where there is an additional local pressure drop caused by a sudden change in the channel geometry (see subsection 3.3 of [46]).

In the flow process, it can be seen that the water arrives at the 90° bend at about $3s$ after the dam failure. Then the water is reflected by the wall to form a front that propagates back towards the reservoir, while the water flow after the 90° bend continues to flow downwards and multiple reflections are observed. The water flow after the 90° bend continues to flow downwards and multiple reflections are observed on the channel walls with the appearance of complicated shapes on a part of the channel. Comparisons between the numerical results and the data collected for a wetted bottom of the measurement gauge points show that the flow arrival time is in good agreement on all gauge points. However, we notice that our FVC scheme captures the water level at gauge point 2 with good accuracy while the SRNH scheme gives different results to the experimental data after $40s$. These results allow us to say that our approach would be able to predict dam failure currents on a vertical step. It also confirms the ability of the FVC scheme to reproduce two-dimensional flows in the presence of a discontinuous front with friction.

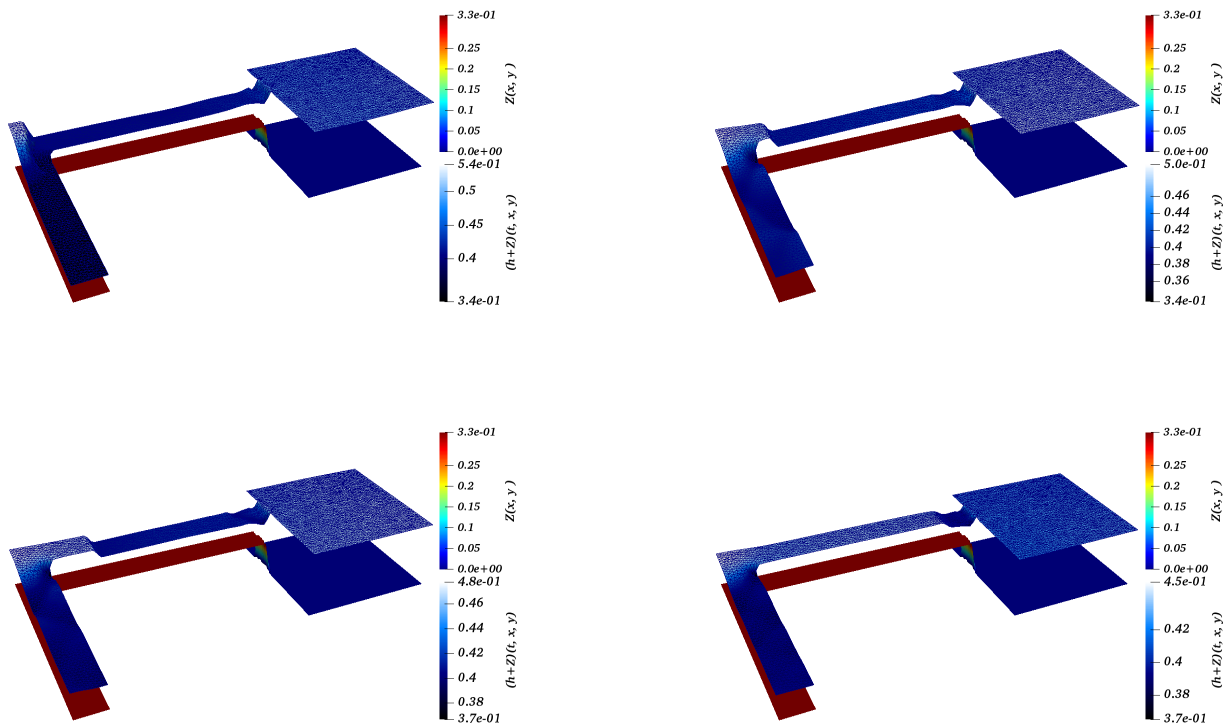


Fig. 30. 3D view of water surface level $h + Z$ and bed profile Z at various times: $t = 3s, t = 5s, t = 7s$, and $t = 14s$

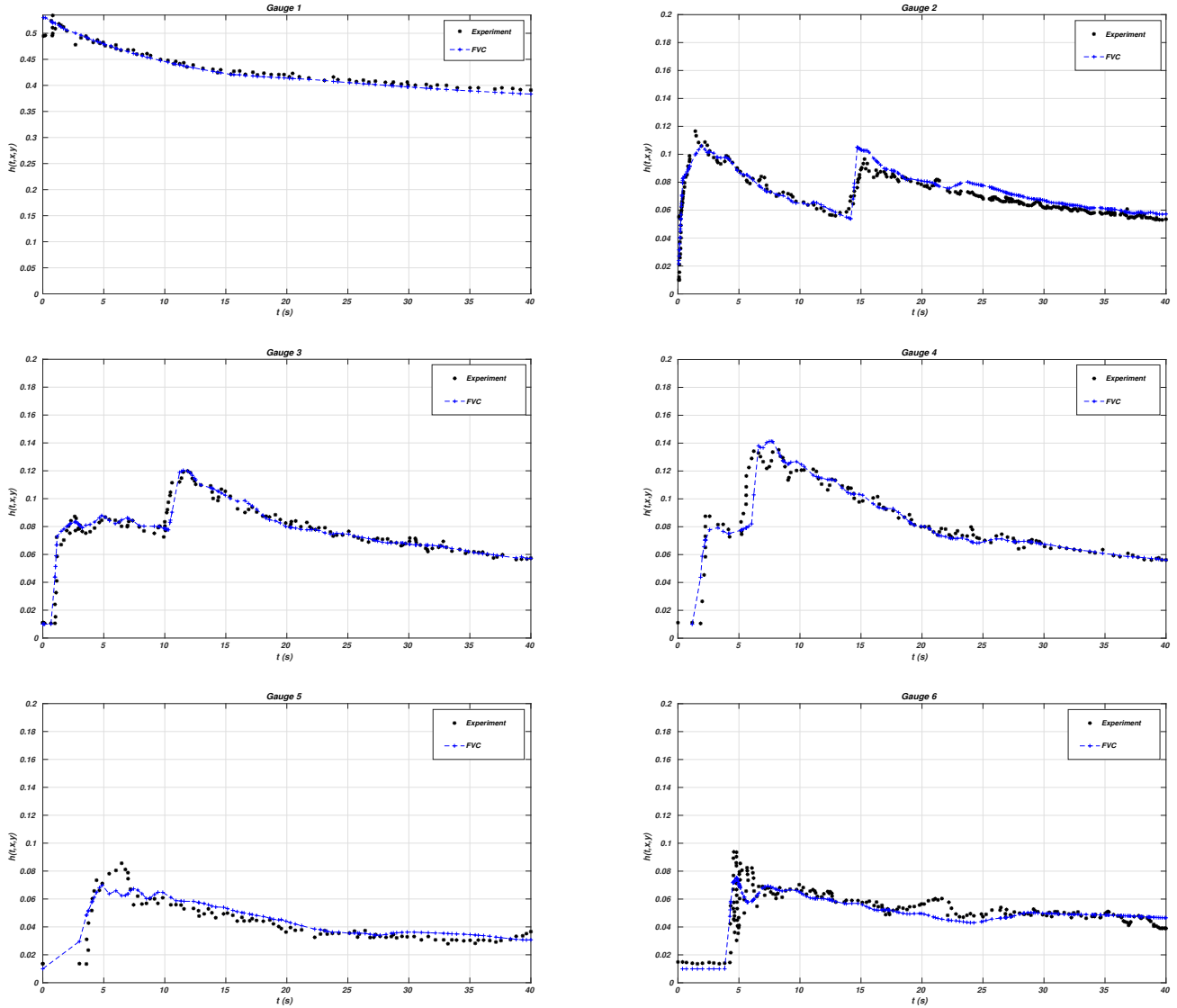


Fig. 31. Comparisons between numerical and experimental data of water depth h at Gauge 1 to 6.

5 Conclusion and perspectives

We have presented in the first part of this paper the extension of the finite volume-characteristics scheme for solving two-dimensional equations of nonlinear conservation laws on unstructured formalism. In the second part, a conservative approach has been presented to approximate the source terms while preserving the stability properties of the homogeneous solver. We note this work was the future goal of many works [17, 16, 47, 48].

Our approach has several advantages, especially solving steady flows without large numerical errors, thus demonstrating that the proposed scheme preserves the balance related to bathymetry term; it can also compute the numerical flux corresponding to the real state of water flow without relying on Riemann problem solvers.

The method's performance has been evaluated for several test examples; furthermore, in [49], the authors concluded the robustness of the finite volume-characteristics method in other types of equations. In this work, we have developed a code for calculating free-surface flows over an irregular bottom for complex geometry. This code is based on the solution of the shallow water equations using the FVC scheme in unstructured meshes. This method applies to problems that represent large source terms due mainly to rapid variation and high background irregularity. Faced with these problems, the methods that use a Riemann approximation solver, which is well suited to the solution of purely hyperbolic equations, often encounter difficulties due to the instability of the numerical solution. In addition to the test cases presented in this paper, there is about fifteen other test cases have been carried out in the context

of free-surface flows; each of these tests aims at verifying precisely one or more properties of our code. It should be noted that some extensions of this approach can be used for modeling realistic applications, notably sediment and pollutant transport. Extending this approximation method to a multi-layer shallow-water model and multi-phase flows [47, 50] will also aim for future works. We can also adapt this method for solving the shallow water magnetohydrodynamic equations [51, 52]. However, it is necessary to mention that at present, our approach is not capable of dealing with the problem of wetting–drying in shallow flows over dry irregular topography; however, there are improvements to be considered in the near future on this issue.

Acknowledgements

The authors thank F. Benkhaldoun, I. El Mahi, and A. Ratnani for fruitful discussions and helpful comments. This work was partially supported by the HPC Project Alkharizmi department, MSDA-UM6P.

Appendix

LS Method

Relations coming from the least square method, which is used in (20)

$$R_x = \sum_{k \in V(c)} (x_k - x_c), \quad R_y = \sum_{k \in V(c)} (y_k - y_c),$$

$$\lambda_x = \frac{I_{xy}R_y - I_{yy}R_x}{I_{xx}I_{yy} - I_{xy}^2}, \quad \lambda_y = \frac{I_{xy}R_x - I_{xx}R_y}{I_{xx}I_{yy} - I_{xy}^2},$$

where,

$$I_{xx} = \sum_{k \in V(c)} (x_k - x_c)^2, \quad I_{yy} = \sum_{k \in V(c)} (y_k - y_c)^2, \quad I_{xy} = \sum_{k \in V(c)} (x_k - x_c)(y_k - y_c)$$

Gradient with the diamond scheme

The calculations leads to (21)

Approximation of the gradient is done on the diamond cell (see Fig.6). One can assume that the gradient of quantity u is constant on the co-volume SRNL. The Green-Gauss theorem consists in writing the following approximation

$$\nabla u_{ij} = \frac{1}{2\mu_{SRNL}} \left\{ (u_S + u_R)\vec{n}_{SR}|\gamma_{SR}| + (u_R + u_N)\vec{n}_{RN}|\gamma_{RN}| + (u_N + u_L)\vec{n}_{NL}|\gamma_{NL}| + (u_L + u_S)\vec{n}_{LS}|\gamma_{LS}| \right\},$$

where u_N , u_S , u_R , and u_L represent respectively the values of the quantity u in the point N , S , R and L .

When we modify the expression inside the square braces, we obtain

$$\nabla u_{ij} = \frac{1}{2\mu_{SRNL}} \left\{ (\vec{n}_{SR}|\gamma_{SR}| + \vec{n}_{LS}|\gamma_{LS}|)u_S + (\vec{n}_{RN}|\gamma_{RN}| + \vec{n}_{NL}|\gamma_{NL}|)u_N + (\vec{n}_{SR}|\gamma_{SR}| + \vec{n}_{RN}|\gamma_{RN}|)u_R \right. \\ \left. + (\vec{n}_{NL}|\gamma_{NL}| + \vec{n}_{LS}|\gamma_{LS}|)u_L \right\},$$

The following equalities are obvious

$$\begin{aligned}\vec{n}_{SR}|\gamma_{SR}| + \vec{n}_{LS}|\gamma_{LS}| &= \vec{n}_{SR}|\gamma_{SR}|, \\ \vec{n}_{RN}|\gamma_{RN}| + \vec{n}_{NL}|\gamma_{NL}| &= -\vec{n}_{LR}|\gamma_{LR}|, \\ \vec{n}_{SR}|\gamma_{SR}| + \vec{n}_{RN}|\gamma_{RN}| &= \vec{n}_{ij}|\gamma_{ij}|, \\ \vec{n}_{NL}|\gamma_{NL}| + \vec{n}_{LS}|\gamma_{LS}| &= -\vec{n}_{ij}|\gamma_{ij}|.\end{aligned}$$

Hence, the formula (21). \square

Exact solution of ideal dam break problem

For each time $t \geq 0$, the analytical solution of ideal dam break without friction is given by

$$h(t, x) = \begin{cases} h_l & \\ \frac{1}{9g} (2\sqrt{gh_l} - \frac{x-x_m}{t}) & \\ h_m & \\ h_r & \end{cases}, \quad u(t, x) = \begin{cases} 0 & \text{if } x \leq x_m - t\sqrt{gh_l}, \\ \frac{2}{3} (\sqrt{gh_l} + \frac{x-x_m}{t}) & \text{if } x_m - t\sqrt{gh_l} \leq x < t(u_m - c_m), \\ u_m & \text{if } t(u_m - c_m) \leq x < x_m + tv_c, \\ 0 & \text{if } x \geq x_m + tv_c. \end{cases}$$

with $v_c = \frac{2c_m^2(\sqrt{gh_l} - c_m)}{c_m^2 - gh_r}$ is the speed of the shock and $c_m = \sqrt{gh_m}$ solution of $8c_m^2 c_l^2 (c_l - c_m)^2 - (c_m^2 - c_r^2)(c_m^2 + c_r^2) = 0$

Relative L^1 error

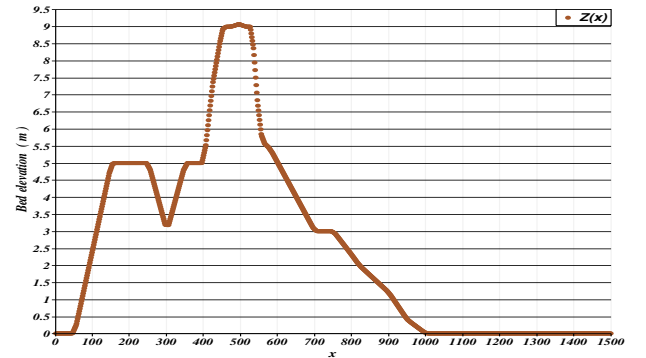
We define the relative error in L^1 norm as follows

$$\frac{\sum_{i=1}^{N_{ele}} |T_i| |h_i^n - h(t_n, x_i, y_i)|}{\sum_{i=1}^{N_{ele}} |T_i| |h(t_n, x_i, y_i)|},$$

where h_i^n and $h(t_n, x_i, y_i)$ are respectively, the computed and exact water depth at the cell T_i , and N_{ele} denotes the total number of cells.

Bed elevation for irregular bed used in 4.3 test

x	0	50	100	150	250	300	350
$Z(x)$	0	0	2.5	5	5	3	5
x	400	425	435	450	475	500	505
$Z(x)$	5	7.5	8	9	9	9.1	9
x	530	550	565	575	600	650	700
$Z(x)$	9	6	5.5	5.5	5	4	3
x	750	800	820	900	950	1000	1500
$Z(x)$	3	2.3	2	1.2	0.4	0	0



References

- [1] Fayssal Benkhaldoun, Salah Daoudi, Imad Elmahi, and Mohammed Seaïd. Numerical modelling of sediment transport in the nador lagoon (morocco). *Applied Numerical Mathematics*, 62(12):1749–1766, 2012.
- [2] Fayssal Benkhaldoun, Imad Elmahi, Saida Sari, and Mohammed Seaïd. An unstructured finite-volume method for coupled models of suspended sediment and bed load transport in shallow-water flows. *International journal for numerical methods in fluids*, 72(9):967–993, 2013.
- [3] EM Chaabelasri, I Elmahi, R Abdellaoui, and N Salhi. Well balanced adaptive simulation of pollutant transport by shallow water flows: Application to the bay of tangier. *International Journal of Hydraulic Engineering*, 3(1):10–23, 2014.
- [4] Stefania Ferrari and Fausto Saleri. A new two-dimensional shallow water model including pressure effects and slow varying bottom topography. *ESAIM: Mathematical Modelling and Numerical Analysis-Modélisation Mathématique et Analyse Numérique*, 38(2):211–234, 2004.
- [5] Fayssal Benkhaldoun, Imad Elmahi, and Mohammed Seaïd. A new finite volume method for flux-gradient and source-term balancing in shallow water equations. *Computer Methods in Applied Mechanics and Engineering*, 199(49-52):3324–3335, 2010.
- [6] Alfredo Bermúdez, Alain Dervieux, Jean-Antoine Desideri, and M Elena Vázquez. Upwind schemes for the two-dimensional shallow water equations with variable depth using unstructured meshes. *Computer methods in applied mechanics and engineering*, 155(1-2):49–72, 1998.
- [7] Alfredo Bermudez and Ma Elena Vazquez. Upwind methods for hyperbolic conservation laws with source terms. *Computers & Fluids*, 23(8):1049–1071, 1994.
- [8] Randall J LeVeque. Balancing source terms and flux gradients in high-resolution godunov methods: the quasi-steady wave-propagation algorithm. *Journal of computational physics*, 146(1):346–365, 1998.
- [9] Tomás Chacón Rebollo, Antonio Domínguez Delgado, and Enrique D Fernández Nieto. An entropy-correction free solver for non-homogeneous shallow water equations. *ESAIM: Mathematical Modelling and Numerical Analysis*, 37(5):755–772, 2003.
- [10] Tomás Chacón Rebollo, Antonio Dominguez Delgado, and Enrique D Fernández Nieto. A family of stable numerical solvers for the shallow water equations with source terms. *Computer methods in applied mechanics and engineering*, 192(1-2):203–225, 2003.
- [11] Manuel J Castro, Sergio Ortega, and Carlos Parés. Well-balanced methods for the shallow water equations in spherical coordinates. *Computers & Fluids*, 157:196–207, 2017.
- [12] Victor Michel-Dansac, Christophe Berthon, Stéphane Clain, and Françoise Foucher. A well-balanced scheme for the shallow-water equations with topography or manning friction. *Journal of Computational Physics*, 335:115–154, 2017.
- [13] Senka Vukovic and Luka Sopta. Eno and weno schemes with the exact conservation property for one-dimensional shallow water equations. *Journal of Computational Physics*, 179(2):593–621, 2002.
- [14] Benoit Perthame and Chiara Simeoni. A kinetic scheme for the saint-venant system with a source term. *Calcolo*, 38(4):201–231, 2001.
- [15] Fayssal Benkhaldoun and Mohammed Seaïd. A simple finite volume method for the shallow water equations. *Journal of computational and applied mathematics*, 234(1):58–72, 2010.
- [16] Fayssal Benkhaldoun, Saida Sari, and Mohammed Seaïd. Projection finite volume method for shallow water flows. *Mathematics and computers in simulation*, 118:87–101, 2015.
- [17] Fayssal Benkhaldoun, Saida Sari, and Mohammed Seaïd. A family of finite volume eulerian–lagrangian methods for two-dimensional conservation laws. *Journal of computational and applied mathematics*, 285:181–202, 2015.
- [18] Jean-Frédéric Gerbeau and Benoît Perthame. Derivation of viscous saint-venant system for laminar shallow water; numerical validation. 2000.
- [19] Olivier Delestre. *Simulation du ruissellement d'eau de pluie sur des surfaces agricoles*. PhD thesis, Université d'Orléans; Université d'Orléans, 2010.
- [20] Jean-Michel Hervouet. *Hydrodynamics of free surface flows: modelling with the finite element method*, volume 360. Wiley Online Library, 2007.
- [21] Sahbi Zaouali. *Structure et modélisation d'écoulements à surface libre dans des canaux de rugosité inhomogène*. PhD thesis, 2008.
- [22] Edwige Godlewski and Pierre-Arnaud Raviart. *Numerical approximation of hyperbolic systems of conservation laws*, volume 118. Springer Science & Business Media, 2013.
- [23] Denis Serre. *Systems of Conservation Laws 1: Hyperbolicity, entropies, shock waves*. Cambridge University Press, 1999.
- [24] Dirk Olbers, Jürgen Willebrand, and Carsten Eden. *Ocean dynamics*. Springer Science & Business Media, 2012.
- [25] Gregor J Gassner, Andrew R Winters, and David A Kopriva. A well balanced and entropy conservative discontinuous galerkin spectral element method for the shallow water equations. *Applied Mathematics and Computation*, 272:291–308, 2016.
- [26] Pierre-Louis Lions, Benoît Perthame, and Panagiotis E Souganidis. Existence and stability of entropy solutions for the hyperbolic systems of isentropic gas dynamics in eulerian and lagrangian coordinates. *Communications on pure and applied mathematics*, 49(6):599–638, 1996.
- [27] Ulrik S Fjordholm, Siddhartha Mishra, and Eitan Tadmor. Well-balanced and energy stable schemes for the shallow water equations with discontinuous topography. *Journal of Computational Physics*, 230(14):5587–5609, 2011.
- [28] Moussa Ziggaf, Mohamed Boubekeur, Fayssal Benkhaldoun, Imad El Mahi, and Imad Kissami. The FVC scheme on unstructured meshes for the two-dimensional shallow water equations. In *International Conference on Finite Volumes for Complex Applications*, pages 455–465. Springer, 2020.

- [29] Philip L Roe. Characteristic-based schemes for the euler equations. *Annual review of fluid mechanics*, 18(1):337–365, 1986.
- [30] Mohammed Seaïd. On the quasi-monotone modified method of characteristics for transport-diffusion problems with reactive sources. *Computational Methods in Applied Mathematics Comput. Methods Appl. Math.*, 2(2):186–210, 2001.
- [31] Ulrik S Fjordholm and Siddhartha Mishra. Vorticity preserving finite volume schemes for the shallow water equations. *SIAM Journal on Scientific Computing*, 33(2):588–611, 2011.
- [32] LA Monthe, F1 Benkhaldoun, and I Elmahi. Positivity preserving finite volume roe: schemes for transport-diffusion equations. *Computer Methods in Applied Mechanics and Engineering*, 178(3-4):215–232, 1999.
- [33] Philip L Roe. Approximate riemann solvers, parameter vectors, and difference schemes. *Journal of computational physics*, 43(2):357–372, 1981.
- [34] Constantine M Dafermos. *Hyperbolic conservation laws in continuum physics*, volume 3. Springer, 2005.
- [35] James J Stoker. The formation of breakers and bores the theory of nonlinear wave propagation in shallow water and open channels. *Communications on Pure and Applied Mathematics*, 1(1):1–87, 1948.
- [36] James Johnston Stoker. *Water waves: The mathematical theory with applications*, volume 36. John Wiley & Sons, 2011.
- [37] FM Henderson. Open channel flow. macmillan series in civil engineering. *New York*, 1966.
- [38] Robert J Fennema and M Hanif Chaudhry. Implicit methods for two-dimensional unsteady free-surface flows. *Journal of hydraulic research*, 27(3):321–332, 1989.
- [39] Emmanuel Audusse, Marie-Odile Bristeau, and Benoit Perthame. *Kinetic schemes for Saint-Venant equations with source terms on unstructured grids*. PhD thesis, INRIA, 2000.
- [40] Robert J Fennema and M Hanif Chaudhry. Explicit methods for 2-d transient free surface flows. *Journal of Hydraulic Engineering*, 116(8):1013–1034, 1990.
- [41] Jian G Zhou, Derek M Causon, Clive G Mingham, and David M Ingram. The surface gradient method for the treatment of source terms in the shallow-water equations. *Journal of Computational physics*, 168(1):1–25, 2001.
- [42] Zhenming Wang, Jun Zhu, and Ning Zhao. A new fifth-order finite difference well-balanced multi-resolution weno scheme for solving shallow water equations. *Computers & Mathematics with Applications*, 80(5):1387–1404, 2020.
- [43] Allen C Kuo and Lorenzo M Polvani. Nonlinear geostrophic adjustment, cyclone/anticyclone asymmetry, and potential vorticity rearrangement. *Physics of Fluids*, 12(5):1087–1100, 2000.
- [44] S Soares Frazão and Y Zech. Dam break in channels with 90 bend. *Journal of Hydraulic Engineering*, 128(11):956–968, 2002.
- [45] M Guan, NG Wright, and PA Sleigh. A robust 2d shallow water model for solving flow over complex topography using homogenous flux method. *International Journal for Numerical Methods in Fluids*, 73(3):225–249, 2013.
- [46] Jian G Zhou, Derek M Causon, David M Ingram, and Clive G Mingham. Numerical solutions of the shallow water equations with discontinuous bed topography. *International journal for numerical methods in fluids*, 38(8):769–788, 2002.
- [47] Emmanuel Audusse, Fayssal Benkhaldoun, Saida Sari, Mohammed Seaïd, and Pablo Tassi. A fast finite volume solver for multi-layered shallow water flows with mass exchange. *Journal of Computational Physics*, 272:23–45, 2014.
- [48] Alia Al-Ghosoun, Michael Herty, and Mohammed Seaïd. A new numerical treatment of moving wet/dry fronts in dam-break flows. *Journal of Applied Mathematics and Computing*, 59(1):489–516, 2019.
- [49] Sutthisak Phongthanapanich and Robert Eymard. A comparative study of characteristic finite element and characteristic finite volume methods for convection-diffusion-reaction problems on triangular grids. *Applied Science and Engineering Progress*, 12(4):235–242, 2019.
- [50] Christopher Earls Brennen and Christopher E Brennen. *Fundamentals of multiphase flow*. 2005.
- [51] Shamsul Qamar and Gerald Warnecke. Application of space–time ce/se method to shallow water magnetohydrodynamic equations. *Journal of computational and applied mathematics*, 196(1):132–149, 2006.
- [52] Saqib Zia, Munshoor Ahmed, and Shamsul Qamar. Numerical solution of shallow water magnetohydrodynamic equations with non-flat bottom topography. *International Journal of Computational Fluid Dynamics*, 28(1-2):56–75, 2014.